

The Surface Edge Explorer (SEE): A measurement-direct approach to next best view planning

Journal Title
XX(X):1–24
©The Author(s) 2022
Reprints and permission:
sagepub.co.uk/journalsPermissions.nav
DOI: 10.1177/ToBeAssigned
www.sagepub.com/

SAGE

Rowan Border¹ and Jonathan D. Gammell¹

Abstract

High-quality observations of the real world are crucial for a variety of applications, including producing 3D printed replicas of small-scale scenes and conducting inspections of large-scale infrastructure. These 3D observations are commonly obtained by combining multiple sensor measurements from different views. Guiding the selection of suitable views is known as the Next Best View (NBV) planning problem.

Most NBV approaches reason about measurements using rigid data structures (e.g., surface meshes or voxel grids). This simplifies next best view selection but can be computationally expensive, reduces real-world fidelity, and couples the selection of a next best view with the final data processing.

This paper presents the Surface Edge Explorer (SEE), a NBV approach that selects new observations directly from previous sensor measurements without requiring rigid data structures. SEE uses measurement density to propose next best views that increase coverage of insufficiently observed surfaces while avoiding potential occlusions. Statistical results from simulated experiments show that SEE can attain better surface coverage in less computational time and sensor travel distance than evaluated volumetric approaches on both small- and large-scale scenes. Real-world experiments demonstrate SEE autonomously observing a deer statue using a 3D sensor affixed to a robotic arm.

Keywords

3D reconstruction, active vision, view planning, next best view, unstructured scene representation, density representation, measurement-direct approach

1 Introduction

Capturing high-fidelity observations of the real world is crucial for performing accurate analysis. High-accuracy scanners attached to industrial robots can be used to compare the structure of manufactured parts with ground-truth production models for quality control. Observations obtained from surveying large-scale outdoor structures, typically with an aerial platform, can be used for infrastructure inspection or to preserve edifices of historical significance. For example, observations of the Notre-Dame de Paris and the ancient city of Palmyra are being used to aid their respective reconstruction efforts.

Obtaining high-quality 3D observations is a challenge regardless of their final purpose. A scene (i.e., a bounded region of space) is observed by combining individual 3D measurements of surfaces obtained from multiple different positions. An observation is complete when there is sufficient measurement coverage on all visible surfaces. The final surface coverage achieved depends on the sensor capabilities, the scene structure, and the views from which measurements are obtained. These views can be chosen by a human operator, but empirically selecting views is often undesirable or impossible.

Algorithmic view selection mitigates human uncertainty by intelligently choosing views. This challenge of planning a *next* view that can provide the *best* improvement in a scene observation is known as the Next Best View (NBV) planning problem. It was first explored by Connolly (1985).

NBV approaches can be broadly categorised by their sources of information. Model-based approaches require prior scene information to plan views (e.g., to compare a manufactured part with its production model) and cannot generalise to unknown scenes. Model-free approaches do not require *a priori* scene information and plan next best views from the current observation state.

The state of an observation is encoded with a scene representation. Most model-free NBV planning approaches use *structured* representations. These impose an external structure onto the scene. Volumetric representations segment the scene volume into a 3D voxel grid. Surface representations create a connected mesh from subsampled sensor measurements. These representations aggregate multiple measurements into each element of their structure. This simplifies selecting next best views but is computationally expensive and reduces observation fidelity. Increasing the structural resolution (e.g., voxel number or mesh density) captures more detail but also increases computational costs. Higher-resolution voxel grids

¹Estimation, Search, and Planning (ESP) Research Group, Oxford Robotics Institute (ORI), Department of Engineering Science, University of Oxford, Oxford, United Kingdom

Corresponding author:

Rowan Border, Oxford Robotics Institute, 23 Banbury Road, Oxford, United Kingdom, OX2 6NN

Email: rborder@oxfordrobotics.institute



Figure 1. A photograph of the UR10 platform. An object (e.g., the Oxford Deer) is placed on a turntable (white) and captured by an Intel RealSense L515 on the UR10 end effector. SEE jointly directs the turntable and UR10 to observe the object.

are more expensive to raycast and denser meshes are more computationally costly to update.

NBV approaches with unstructured representations do not impose external structures onto the scene and reason directly about sensor measurements. This maintains full fidelity and does not require restrictive assumptions about the scene structure but does require NBV approaches to reason about sensor measurements.

The Surface Edge Explorer (SEE) proposes next best views directly from measurement density. It identifies surfaces with low measurement density and proposes views to capture additional measurements. These views can be refined to avoid occlusions and improve visibility of their target surfaces. The next best view is chosen from these proposals to obtain a significant improvement in scene coverage while moving a short distance. New views are captured until a minimum measurement density is captured from the entire scene. The efficiency of this measurement-direct method allows SEE to obtain complete observations with relatively short travel distances and observation times compared to state-of-the-art volumetric approaches.

The observation performance of SEE is evaluated with both simulated and real-world experiments. The simulation experiments provide a quantitative comparison of SEE with state-of-the-art volumetric approaches on both small- and large-scale scenes. In one simulation, small-scale tabletop models are observed using an RGB-D camera attached to a robotic arm. In another simulation, large-scale building models are observed with a LiDAR mounted on an aerial platform. SEE consistently outperforms the evaluated volumetric approaches in these simulation experiments by obtaining similar or better surface coverage while travelling shorter distances and requiring less observation time.

Real-world experiments demonstrate the same observation performance on a physical robotic platform (Fig. 1). The experimental platform is comprised of a turntable, onto which observation targets are placed, and a UR10 robot arm with an Intel RealSense L515 affixed to the end effector. The observation target used for the real-world experiments was a deer statue, known as the Oxford Deer. Results from these real-world experiments show that SEE can obtain high-quality observations of the Oxford Deer with similar performance to the simulations, despite sensor noise (Fig. 2).



Figure 2. A pointcloud of the Oxford Deer captured by SEE using the UR10 platform.

1.1 Statement of Contributions

This paper presents a definitive version of SEE and evaluates its observation capabilities in simulation and the real world. SEE and its unstructured density representation were first presented in Border et al. (2017) and extended in Border et al. (2018), Border (2019) and Border and Gammell (2020). This paper makes the following specific contributions:

- Presents a definitive version of SEE that unifies previously published work and extends it to improve performance and remove user-specified parameters.
- Uses realistic simulations of both small- and large-scale scenes to compare the observation performance of SEE with state-of-the-art volumetric approaches.
- Demonstrates that SEE can capture highly complete scene observations using less travel distance and observation time than the volumetric approaches.
- Presents the first evaluation of SEE working with a fully autonomous real-world system.
- Illustrates that SEE can efficiently obtain high-quality observations of a real-world object using a 3D sensor.

2 Background

This section presents an overview of the NBV planning problem (Section 2.1) and a review of relevant literature on model-free approaches. Different strategies for categorising NBV planning approaches have been presented in survey papers (Tarabani et al. 1995; Scott et al. 2003; Karaszewski et al. 2016a; Zeng et al. 2020). This review adopts the classification scheme used by Scott et al. (2003) to discuss approaches based on their scene representation.

Approaches using volumetric representations are reviewed in Section 2.2, those with surface representations are discussed in Section 2.3 and approaches that utilize a combination of multiple representations are considered in Section 2.4. A new class of unstructured scene representations, which includes the density representation used by SEE, is introduced in Section 2.5.

2.1 The Next Best View Planning Problem

The challenge of NBV planning is proposing and selecting views from which a scene can be efficiently observed. The quality of an observation can be quantified by its accuracy (i.e., how closely the captured data resembles the actual scene) and completeness (i.e., what proportion of the scene

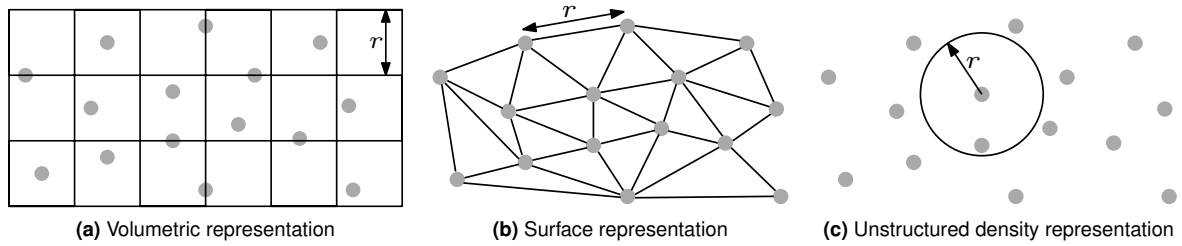


Figure 3. Illustrations of (a) a volumetric scene representation (i.e., a voxel grid), (b) a surface representation (i.e., a connected mesh) and (c) the unstructured density representation presented in this paper. A resolution parameter, r , defines the voxel size for a volumetric representation, the maximum edge length for a surface representation or the search radius for the density representation.

has been observed). Observation accuracy primarily depends on the sensor capabilities but can be improved by considering the scene texture and geometry. The completeness of an observation is determined by the coverage obtained from captured views. The efficiency of a NBV approach is quantified by the computation time and sensor travel distance required to obtain an observation.

Approaches to the NBV planning problem select views by evaluating information obtained from previous views and in some cases *a priori* scene information. The problem can be formally expressed as a function, $\mathbf{v}' = \text{nbv}(V, Y)$, which selects a view, \mathbf{v}' , from a (possibly uncountable) set of potential views, V , based on information obtained from previous views or *a priori* scene information, Y . A next best view is selected to provide the greatest observation improvement by evaluating a set of quantitative metrics, $\text{metrics}(\mathbf{v}, Y)$,

$$\mathbf{v}' = \text{nbv}(V, Y) = \arg \max_{\mathbf{v} \in V} \text{metrics}(\mathbf{v}, Y).$$

Each captured view improves the scene information available for selecting subsequent next best views. The representation chosen to encode this information is a defining characteristic of NBV algorithms. Volumetric representations segment the scene volume into a three-dimensional voxel grid (Fig. 3a). Surface representations connect sensor measurements to create a surface mesh (Fig. 3b). Some NBV planning approaches also encode scene information using a combination of these volumetric and surface representations. Unstructured representations, such as the density representation presented in this paper, do not impose an external structure on the scene or assume any connectivity between sensor measurements (Fig. 3c).

2.2 Volumetric Representations

NBV planning approaches most commonly use a *volumetric* representation for encoding scene information. This representation divides the scene volume into three-dimensional cells known as voxels. A state associated with each voxel encodes information on its observation status and occupancy. The visibility of voxels from a set of views is evaluated by raycasting into the voxel grid from each potential view and recording the states of voxels intersected by the rays. A value for each view is determined from the intersected voxel states.

Approaches using a volumetric representation can be broadly separated into three categories based on their method

for proposing views. Many approaches use a predefined set of views chosen from a surface (e.g., a sphere or hemisphere) encompassing the scene (Section 2.2.1). Some approaches use path planning methods to propose views within free space regions of the scene (Section 2.2.2). Other approaches propose views using scene information obtained from the occupancy and observation states of voxels (Section 2.2.3).

2.2.1 Selecting Views From a Predefined Set Volumetric approaches that select views from a predefined set are primarily differentiated by how they use the measurement information encoded in their voxel representation.

Connolly (1985) coined the term *next best view* in formative work which presents the first approaches to the NBV problem. One approach uses a fixed set of view proposals chosen from the surface of a sphere encompassing the scene. Voxels are classified by their occupancy and observation states. Next best views are selected to capture the most unobserved voxels. Some subsequent NBV works (Papadopoulos-Orfanos and Schmitt 1997; Wong et al. 1999) use the same voxel classifications and next best view selection metric but different view proposal sets (e.g., using the centers of empty voxels). These approaches prioritise capturing unobserved voxels and consider occlusions caused by occupied voxels but do not explicitly classify occluded voxels or evaluate the quality of captured measurements.

Several approaches extend this work by classifying occluded voxels and considering observation quality. Banta et al. (2000) introduce an occluded classification for voxels that lie within a viewing frustum but are obscured by occupied voxels. Next best views are selected to observe the most occluded voxels. Massios and Fisher (1998) identify unobserved voxels with at least one unoccupied neighbour and refer to them as *ocplane* voxels. Next best views with orientations parallel to voxel-based surface normals are chosen to improve observation quality.

Vasquez-Gomez et al. (2009, 2014) present an approach that combines the occluded and ocplane voxel classifications with a NBV selection metric that considers observation quality. These approaches obtain more reliable measurements from a greater number of unobserved voxels by explicitly considering occlusions and observation quality; however, the use of binary voxel occupancy states can result in scene regions being sparsely covered by captured measurements.

Some limitations of binary voxel states can be addressed with a probabilistic voxel representation. This defines voxel occupancy as the likelihood that a voxel should contain sensor measurements. NBV approaches using this

representation select next best views with Information Gain (IG) metrics. These quantify the value of a view by evaluating the expected information of likely visible voxels. Potthast and Sukhatme (2014) use an IG metric to quantify the visibility of unobserved voxels from views and select a next best view to have the highest IG. Isler et al. (2016) and Delmerico et al. (2018) present several IG-based view selection metrics that consider the occupancy probability, visibility and distance of voxels from a view. Abduldayem et al. (2017) and Almadhoun et al. (2019) present an approach that uses knowledge of geometric symmetry in a scene to predict voxel occupancy.

Krainin et al. (2011) use occupancy probabilities to create an implicit Truncated Signed Distance Field (TSDF) surface (Curless and Levoy 1996) and select next best views to reduce its uncertainty. Hou et al. (2019) present a method that improves upon the accuracy of independent per-voxel occupancy probabilities by using a Markov Chain Monte Carlo (MCMC) Gibbs sampler to jointly estimate occupancy probabilities for the entire voxel grid. Lauri et al. (2019, 2020) present a multi-sensor approach that chooses a set of next best views to jointly maximise an IG metric while reducing unnecessary overlap between the views. These probabilistic approaches are able to obtain observations with more consistent scene coverage due to the greater fidelity of their voxel representations.

Some recent works have applied deep learning to the NBV problem. Wang et al. (2019) train a Convolutional Neural Network (CNN) to select next best views with the greatest number of visible occupied voxels. Mendoza et al. (2020) train a CNN to select views that can provide the greatest increase in scene coverage while satisfying overlap constraints. These approaches can obtain highly complete observations of scenes with geometry similar to the training sets but do not generalise to scenes with unseen geometry.

Many volumetric approaches that choose views from a predefined set are capable of obtaining observations with high coverage of the scene volume; however, the completeness of these observations depends on the distribution of the predefined views since high coverage of the scene volume does not ensure good surface visibility.

2.2.2 Sampling Views With Path Planning Other volumetric approaches use path planning techniques to generate views in the free space of a scene. Views are proposed at the states sampled by the planning algorithm and evaluated when selecting a next best view.

Some approaches use path planners to sample views from the entire scene volume. This enables them to obtain high global scene coverage but it is computationally expensive to raycast a large number of views. Potthast and Sukhatme (2011) use a Probabilistic Roadmap (PRM; Kavraki et al. 1996) to sample potential views. Yoder and Scherer (2016) sample views around a scene with the SPARTAN path planner (Cover et al. 2013).

Many approaches reduce the cost of raycasting views by limiting their view sampling to a local region around the current sensor position. New views are sampled whenever the sensor moves to a chosen next best view. Most of these approaches use Rapidly-exploring Random Trees (RRT; LaValle 1998) or RRT* (Karaman and Frazzoli 2011).

Vasquez-Gomez et al. (2018) use RRT to sample views in the state space of a robotic platform, extending earlier work by Vasquez-Gomez et al. (2017) that uses random sampling.

Bircher et al. (2016, 2018) use RRT to iteratively sample potential views. An RRT is grown from the current sensor position into unoccupied voxel space. Each vertex in the tree is assigned an IG value based on the total volume of visible unobserved voxels. The cumulative IG value of each branch is computed and a next best view is chosen to be the first vertex along the branch with the highest IG. Observations captured by these iterative approaches can be highly complete in local scene regions but do not typically obtain good global coverage.

Recent works introduce methods to obtain high global scene coverage with a reduced computational cost. Selin et al. (2019) extends Bircher et al. (2016, 2018) by preserving high-value views between sampling iterations and evaluating view value with an efficient sparse raycasting method. Schmid et al. (2019) further improve this approach by using RRT* to iteratively expand a single exploration tree when sampling new views.

Volumetric approaches that sample view proposals using path planning techniques can typically obtain greater scene coverage than those using a predefined set of views. The sampled views have better visibility of scene surfaces since they are distributed throughout the scene volume instead of around it. A limitation of this method is the computational cost of raycasting the large number of sampled views.

2.2.3 Proposing Views Using Scene Information Volumetric approaches that use the current voxel states to propose views can capture high-quality observations with greater efficiency than other volumetric methods. Their observations are often more efficient as higher quality views are proposed and fewer views need to be considered.

The most naive version of this method proposes views in unoccupied voxels. The views can be randomly sampled (Palomeras et al. 2019) or placed at specific locations (e.g., voxel centers; Potthast and Sukhatme 2014; Daudelin and Campbell 2017). These approaches are unlikely to obtain higher quality observations as they do not consider the observed scene geometry when proposing views but may achieve lower computation times by evaluating fewer views.

The highest quality observations are captured when views are proposed using the observed scene geometry. Some volumetric approaches achieve this by proposing views to capture unobserved voxels with occupied neighbours (i.e., frontier voxels). Early approaches (Connolly 1985; Wong et al. 1999) directly propose a next best view by counting the number of frontier voxels visible from each side of a cubic scene volume and generating a view at the corner with the greatest total visibility. More recent approaches (Monica and Aleotti 2018a; Hardouin et al. 2020a,b) identify clusters of frontier voxels and compute a normal for each cluster from an implicit TSDF surface. The normal for each cluster is used to propose a view of its frontier voxels. A next best view is selected to observe the largest frontier cluster.

Volumetric approaches that use the current voxel states to propose views can obtain higher quality observations with greater efficiency than other volumetric methods. Computational cost is reduced as only views proposed to

improve an observation are evaluated with raycasting. More accurate measurements are obtained by leveraging the scene geometry to propose views with better surface visibility; however, the volumetric structure limits the magnitude of these improvements as raycasting remains computationally expensive and the fidelity of scene information is still limited by the voxel resolution.

2.3 Surface Representations

Approaches with *surface* representations approximate the scene geometry by creating a connected mesh from sensor measurements. This mesh can provide high-fidelity information about the scene structure for proposing views, selecting a next best view and evaluating observation quality. Mesh boundaries can be used to quantify scene coverage and occlusions can be identified by raycasting the mesh.

Most surface approaches require multiple data capture stages to obtain complete scene observations. An initial observation creates a coarse mesh from sparse measurements by following a preplanned or human-directed view trajectory. This initial mesh is then refined by integrating measurements from a second NBV-planning-directed observation.

Reed and Allen (2000) select next best views to observe occluded surfaces in a mesh representation. This improves the measurement density on surfaces with irregular geometry and refines the initial mesh observation. Hollinger et al. (2012) model uncertainty in the initial mesh using Gaussian process implicit surfaces. Views are proposed to observe each point in the mesh and next best views are chosen to provide the greatest reduction in uncertainty. Roberts et al. (2017) propose views by independently sampling sets of view positions and orientations. The value of each view is defined by the visibility of vertices in the initial mesh. An optimised view trajectory maximises the additive value of each view visited while satisfying a distance constraint.

Peng and Isler (2019) account for the scene geometry when proposing views by sampling them from a manifold encompassing the scene. This manifold is produced by moving each vertex in the initial mesh a given distance along its surface normal and computing a convex hull from the resulting points. All these two-stage approaches are able to capture high quality observations by using knowledge of the scene geometry obtained from the initial survey, but requiring an extra capture stage increases the overall observation time.

Khalifaoui et al. (2013) present a surface-based approach that does not require a multistage observation but is restricted to observing scenes with smooth geometry. The visibility of surfaces in the current mesh is classified based on the angles between their normals and the sensor pose. Views are proposed to observe surfaces with poor visibility. A next best view is chosen to observe the greatest area of poorly visible surfaces.

Surface approaches can typically capture higher quality scene observations than volumetric approaches by considering the scene geometry when proposing and selecting views; however, requiring multiple observation stages increases the overall capture time and creating a mesh from dense sensor measurements is often computationally expensive.

2.4 Combined Representations

Approaches with *combined* representations aim to leverage the advantages of multiple representation types and mitigate their limitations. Most combine volumetric and surface representations to utilise information on both voxel observation states and the scene geometry.

Kriegel et al. (2012, 2015) present a combined approach with a probabilistic voxel grid by extending earlier work using a surface representation (Kriegel et al. 2011). Views are proposed to extend the boundaries of a surface mesh. They are assigned an IG view value computed from the voxel grid. Next best views are chosen to have the highest IG.

Song and Jo (2018) and Song et al. (2020) extend earlier work on a volumetric approach (Song and Jo 2017) with a surface representation. Potential views are sampled with RRT* and a next best view is selected to capture the most unobserved voxels. The surface representation is obtained by extracting an implicit TSDF surface from the voxel grid and using it to create an explicit Poisson reconstruction (Kazhdan et al. 2006). Additional views are sampled between the current sensor position and the next best view. A trajectory is planned between the sampled views to observe uncertain surfaces in the reconstruction and the most frontier voxels.

Some combined approaches also consider measurement density. Low and Lastra (2006) represent scene observations with a combination of voxels and surface patches. Their approach aims to obtain a minimum measurement density within each occupied voxel. Measurements in voxels with insufficient density are connected to define surface patches. Views are proposed to observe these patches and a next best view is selected to observe the patch that offers the greatest potential increase in measurement density.

Karaszewski et al. (2016b) present a multistage combined approach. The first stage, originally presented by Karaszewski et al. (2012), uses a volumetric representation with a density-based measurement classification to propose and select views of scene regions with insufficient measurements. A Poisson surface reconstruction is created from this initial observation and then refined by capturing more views.

Some approaches present novel hybrid representations. Dierenbach et al. (2016) use the Growing Neural Gas (GNG) algorithm (Fritzke 1994) to learn a model of the scene geometry from sensor measurements. This model defines a graph of connected nodes similar to a mesh representation. The scene volume is partitioned into a Voronoi tessellation where each node lies at the centre of a Voronoi cell. Views are proposed to observe each node. A next best view is selected to observe the cell with the lowest measurement density.

Monica and Aleotti (2018b) present an approach with a novel surfel representation. Surfels are circular disks defined by a position, radius and normal. They are extracted from an underlying volumetric representation. Surfels that lie on the boundary between unobserved and unoccupied voxels are classified as frontels. Next best views are selected to observe the set of visible frontels with the greatest surface area.

Approaches with combined representations can obtain more complete and accurate scene observations than other approaches by leveraging the advantages of multiple representations; however, a greater computational cost is typically incurred for maintaining several representations.

2.5 Unstructured Representations

Many of the limitations associated with structured scene representations can be overcome by using an *unstructured* representation. These directly represent the observation state using sensor measurements instead of encoding scene information in an external structure. There is no reduction in the fidelity of scene information and no extra computational cost is incurred for maintaining an external structure.

SEE is the first NBV approach to use a fully unstructured representation, to the best of our knowledge, but other unstructured approaches have since been presented. Peralta et al. (2020) and Zeng et al. (2020) use machine-learning based methods with a pointcloud representation to select next best views that can provide the greatest improvements in scene coverage. These can obtain good observations of structures similar to their training sets but do not generalise well to unseen geometry.

Arce et al. (2020) present a multistage approach with a density-based measurement classification similar to SEE. An initial scene observation is obtained by moving the sensor along a fixed trajectory. Boundary points in the resulting pointcloud are identified using a density-based classification and grouped into clusters. A view is proposed to observe each cluster by estimating the local surface normal and a trajectory between them is found. While this approach is shown to obtain good observations, unlike SEE it requires a manual initial observation and lacks consideration for scene coverage when planning views.

SEE is a measurement-direct NBV approach with an unstructured density representation. It represents all scene information with a point-based encoding and therefore avoids the computational cost of maintaining an external structure (i.e., a voxel grid or surface mesh). The density representation only requires local point-wise computations to evaluate an observation. These methods are more efficient than the raycasting used by volumetric approaches and the mesh analysis techniques utilised by surface approaches.

The fidelity of scene information is not constrained by a structural resolution as captured measurements are individually classified based on density of neighbouring points. SEE leverages this detailed knowledge to identify scene regions that require further observation, propose views that avoid occlusions and select next best views that can obtain the best improvements in surface coverage. This enables it to observe scenes with greater efficiency and often higher completion than structured approaches, whose performance is constrained by their structural resolution.

3 The Surface Edge Explorer (SEE)

This paper presents SEE, a NBV planning approach with an unstructured density representation. SEE aims to obtain complete scene observations by capturing a minimum measurement density from all visible surfaces. Sensor measurements are individually classified by the number of neighbouring points within a resolution radius (Section 3.1).

This density-based classification of measurements is used to identify the *frontiers* between sufficiently and insufficiently observed surfaces (Section 3.2). Views are then proposed to observe the surfaces at these frontiers (Section 3.3). Known occlusions are handled proactively

Algorithm 1 SEE($\mathbf{v}_0, r, \rho, d, \epsilon, \psi, v, \tau, \omega_x, \omega_y, \theta_x, \theta_y$)

```

1:  $P \equiv P_c \cup P_f \cup P_o$ ;  $\mathcal{G} \equiv (M, K)$ 
2:  $P', P_c, P_f, P_o, V, M, K = \emptyset$ ;  $k_{\min} = 0$ 
3:  $\mathbf{v}_c \leftarrow \mathbf{v}_0$ ;  $\mathbf{f}_c \leftarrow \text{NULL}$ ;  $X_{\text{cap}} \leftarrow \text{NULL}$ ;  $E_{\text{surf}} \leftarrow \text{NULL}$ 
4: SetParameters( $r, \rho, d, \epsilon, k_{\min}, \omega_x, \omega_y, \theta_x, \theta_y$ )
5: repeat
6:   GetNewMeasurements( $\mathbf{v}_c, P'$ )
7:   ClassifyPoints( $\mathbf{v}_c, P', P_c, P_f, P_o, X_{\text{cap}}$ )
8:   if  $\mathbf{f}_c \in P_f$  then
9:     AdjustView( $\mathbf{v}_c, \mathbf{f}_c, P', P_f, P_o, V, X_{\text{cap}}, E_{\text{surf}}$ )
10:  end if
11:  ProposeViews( $\mathbf{v}_c, P, P', P_f, V, E_{\text{surf}}$ )
12:  RefineViews( $\mathbf{v}_c, P, P_f, P_o, V, X_{\text{cap}}, E_{\text{surf}}$ )
13:  GraphViews( $\mathbf{v}_c, P_f, V, \mathcal{G}$ )
14:  SelectNBV( $\mathbf{v}_c, \mathbf{f}_c, \mathcal{G}$ )
15: until  $P_f = \emptyset$ 
16: return complete

```

by detecting occluding points before a view is obtained and proposing an alternative unoccluded view (Section 3.4). The visibility of surfaces from views is quantified by encoding the shared visibility of frontier points from views in a graphical representation (Section 3.5). Next best views are chosen from this graph to obtain significant improvements in surface coverage while reducing travel distance (Section 3.6). If a target frontier point is not observed from a view — typically due to an unknown occlusion or surface discontinuity — then it is reactively adjusted to avoid the obstruction (Section 3.7). New views are captured until there are no frontier points remaining (Section 3.8).

Algorithm 1 presents an overview of SEE. The observation parameters are set using user-specified values and the sensor properties (Line 4). New measurements are iteratively obtained and processed to select a next best view (Line 5). A set of new measurements, P' , is captured from a sensor at the current view, \mathbf{v}_c (Line 6). These measurements are added to the SEE pointcloud, P , and the classifications of core, P_c , frontier, P_f , and outlier, P_o , points are updated (Line 7). If the target frontier point associated with the current view, \mathbf{f} , was not successfully observed (i.e., it is still classified as a frontier point) then the view is adjusted (Lines 8–10). New views are proposed to observe the new frontier points and added to the set of view proposals, V (Line 11). The τ -nearest view proposals to the current view are proactively checked for occlusions and refined if necessary (Line 12). The connectivity of these views in the frontier visibility graph, \mathcal{G} , is then updated by evaluating their shared visibility of frontier points (Line 13). A next best view is selected from this graph and the sensor is moved to capture new measurements (Line 14). The observation completes when there are no frontiers remaining (Lines 15–16).

3.1 Setting Parameters

SEE aims to obtain scene observations with a minimum measurement density over all visible surfaces. This measurement density, ρ , is calculated within an r -radius sphere. Sensor measurements are captured at a view distance, d , and separated by a minimum distance, ϵ . These parameters can be user-specified or computed from other parameters

Table 1. The configuration parameters of SEE.

Parameter	Description	Units
ρ	Target measurement density	points per m ³
r	Resolution radius	m
d	View distance	m
ϵ	Minimum separation distance	m
ψ	Occlusion search distance	m
v	Visibility search distance	m
τ	Maximum views to update	number of views

Algorithm 2 SetParameters($r, \rho, d, \epsilon, k_{\min}, \omega_x, \omega_y, \theta_x, \theta_y$)

```

1: if  $r = 0$  and  $\rho \neq 0$  then
2:    $r \leftarrow \left( \frac{9}{4\pi\rho} \right)^{\frac{1}{3}}$ 
3: end if
4: if  $\rho = 0$  and  $d \neq 0$  and  $r \neq 0$  then
5:    $\rho \leftarrow \frac{\omega_x \omega_y}{4 \tan 0.5\theta_x \tan 0.5\theta_y (3d^2 + 2r^2)}$ 
6: end if
7: if  $d = 0$  and  $\rho \neq 0$  and  $r \neq 0$  then
8:    $d \leftarrow \sqrt{\frac{\omega_x \omega_y}{12\rho \tan 0.5\theta_x \tan 0.5\theta_y} - \frac{2r^2}{3}}$ 
9: end if
10: if  $\epsilon = 0$  then
11:    $\epsilon \leftarrow \left( \frac{3r}{2\pi\rho} \right)^{\frac{1}{3}}$ 
12: end if
13:  $k_{\min} \leftarrow \left\lceil \frac{4}{3} \pi \rho r^3 \right\rceil$ 

```

and the sensor properties. Table 1 presents the configurable parameters used by SEE.

The target measurement density, ρ , determines how many measurements need to be captured from scene surfaces. It should be set sufficiently high to attain the desired level of structural detail from a scene. The resolution radius, r , defines the scale at which the measurement density is evaluated. This should be large enough to handle measurement noise robustly while still retaining surface features and computational efficiency. The view distance, d , sets the range at which a sensor observes the scene. It should be set so that sufficient frontier points can be identified from captured measurements. If the view distance is too large, the measurements will be sparsely distributed over scene surfaces and may all be outlier points. When the sensor is too close, the measurements will be densely distributed over surfaces and may all be core points. The minimum separation distance, ϵ , between measurements is used to reduce memory consumption and computational cost. It should be set small enough that it does not affect point classification. Algorithm 2 presents the calculation of these parameters from the sensor resolution, ω_x and ω_y , and field-of-view, θ_x and θ_y .

If the user specifies a value for the target density but not the resolution radius then it is computed such that the resulting volume will contain three points at the target density (Lines 1–3). If the resolution radius and view distance parameters are set, but the target density is not, then it is calculated from the sensor properties to equal the density of sensor measurements that could be captured from the

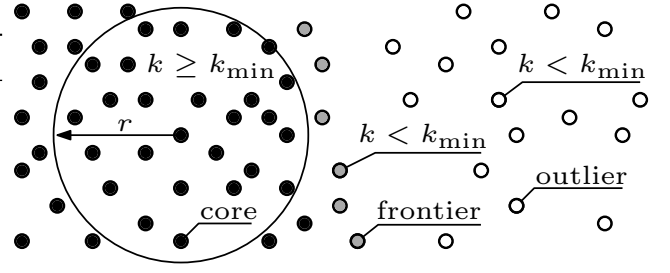


Figure 4. An illustration of the density-based classification used by SEE (Alg. 3). Measurements with a sufficient number of neighbours, k_{\min} , in an r -radius are classified as core (black) while those without are outliers (white). Outlier measurements with core neighbours are frontiers (grey).

largest observable surface area at the specified view distance (Lines 4–6). If the target density and resolution radius are set but not the view distance then it is computed such that the measurement density captured from the largest observable surface area would be equal to the target density (Lines 7–9).

If the minimum separation distance is not specified then a suitable value is computed from the target density and resolution radius (Lines 10–12). The final parameter, k_{\min} , is not user-configurable and defines the number of points that need to exist in an r -radius sphere with density ρ (Line 13).

The remaining user-specified parameters tune the practical performance of SEE. The occlusion search distance, ψ , is the radius around a frontier point that is searched for occluding points. It should ideally be equal to the view distance to capture all occluding points but can be reduced to limit computational cost. The visibility search distance, v , is the radius around the sight line of a view that is searched for occluding points. It should be large enough that an unoccluded view is able to successfully observe new measurements around its associated frontier. The maximum views to update, τ , defines the number of neighbouring views that are processed when handling occlusions and updating the frontier visibility graph. It should be as high as possible without incurring a significant computational cost.

3.2 Processing Sensor Measurements

Sensor measurements are classified based on the number of neighbouring points within the resolution radius (Fig. 4). Measurements with more neighbours than specified by the target density are classified as *core* points and those without are classified as *outlier* points. Outlier points with core neighbours are classified as *frontier* points. These frontiers define a boundary between sufficiently and insufficiently observed surfaces.

New sensor measurements are processed by adding them to the SEE pointcloud and assigning a classification. The density-based classification approach is based on Density-Based Spatial Clustering of Applications with Noise (DBSCAN; Ester et al. 1996). Sensor measurements, $P := \{\mathbf{p}_i\}_{i=1}^n$, where $\mathbf{p}_i \in \mathbb{R}^3$, are classified as core points, P_c , frontier points, P_f , or outlier points, P_o . The point classifications are complete and unique so that every point is assigned to a single class; i.e.,

$$P = P_c \cup P_f \cup P_o$$

and

Algorithm 3 ClassifyPoints($\mathbf{v}_c, P', P_c, P_f, P_o, X_{cap}$)

```

1:  $\mathbf{v}_c \equiv (\mathbf{x}_c, \phi_c)$ ;  $P \equiv P_c \cup P_f \cup P_o$ 
2:  $R \leftarrow \emptyset$ 
3: for all  $\mathbf{p} \in P'$  do
4:   if  $\text{Neighbours}_r(P, \epsilon, \mathbf{p}) = \emptyset$  then
5:      $P \leftarrow P \cup \{\mathbf{p}\}$ 
6:      $Q \leftarrow \{\mathbf{p}\} \cup \text{Neighbours}_r(P, r, \mathbf{p})$ 
7:      $X_{cap}[\mathbf{p}] \leftarrow \mathbf{x}_c$ 
8:     for all  $\mathbf{q} \in Q$  do
9:       if  $\mathbf{q} \notin P_c$  then
10:         $N_q \leftarrow \text{Neighbours}_r(P, r, \mathbf{q})$ 
11:        if  $|N_q| < k_{\min}$  then
12:          if  $N_q \cap P_c \neq \emptyset$  then
13:             $P_f \leftarrow P_f \cup \{\mathbf{q}\}$ 
14:            if  $\mathbf{q} \in P_o$  then
15:               $P_o \leftarrow P_o \setminus \{\mathbf{q}\}$ 
16:            end if
17:          else
18:             $P_o \leftarrow P_o \cup \{\mathbf{q}\}$ 
19:          end if
20:        else
21:           $P_c \leftarrow P_c \cup \{\mathbf{q}\}$ 
22:          if  $\mathbf{q} \in P_f$  then
23:             $P_f \leftarrow P_f \setminus \{\mathbf{q}\}$ 
24:          end if
25:          if  $\mathbf{q} \in P_o$  then
26:             $P_o \leftarrow P_o \setminus \{\mathbf{q}\}$ 
27:          end if
28:          if  $\mathbf{p} \neq \mathbf{q}$  and  $\mathbf{q} \notin R$  then
29:             $Q \leftarrow Q \cup N_q$ 
30:             $R \leftarrow R \cup \{\mathbf{q}\}$ 
31:          end if
32:        end if
33:      end if
34:    end for
35:  end if
36: end for

```

$$P_c \cap P_f = P_c \cap P_o = P_f \cap P_o = \emptyset.$$

The set of measurements, $N_{\mathbf{p}}$, in the pointcloud within an r -radius of a point, \mathbf{p} , is given by

$$N_{\mathbf{p}} := \text{Neighbours}_r(P, \mathbf{p}) := \{\mathbf{q} \in P \mid \|\mathbf{q} - \mathbf{p}\| \leq r\},$$

where $\|\cdot\|$ denotes the L^2 -norm.

A point is classified as core if it has at least k_{\min} neighbours,

$$P_c := \{\mathbf{p} \in P \mid |N_{\mathbf{p}}| \geq k_{\min}\},$$

where $|\cdot|$ denotes set cardinality.

A point is classified as a frontier if it has fewer than k_{\min} neighbours, some of which are core points,

$$P_f := \{\mathbf{p} \in P \mid |N_{\mathbf{p}}| < k_{\min} \wedge N_{\mathbf{p}} \cap P_c \neq \emptyset\},$$

or as an outlier otherwise,

$$P_o := \{\mathbf{p} \in P \mid |N_{\mathbf{p}}| < k_{\min} \wedge N_{\mathbf{p}} \cap P_c = \emptyset\}.$$

Algorithm 3 presents the classification of new measurements. Each point in the set of new measurements, $\mathbf{p} \in P'$, is processed (Line 3). Any point that satisfies the ϵ -radius constraint is added to the SEE pointcloud, P , and the (re)classification queue, Q , along with its neighbourhood

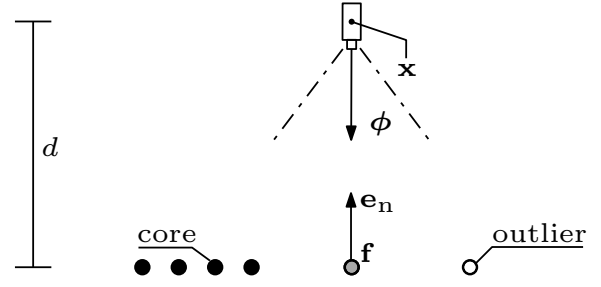


Figure 5. An illustration of a view proposal (Alg. 4). A view, $\mathbf{v} \equiv (\mathbf{x}, \phi)$, is proposed to observe the surfaces around a target frontier point (grey dot), f , using the locally estimated surface normal, e_n . The view position, \mathbf{x} , is set at the view distance, d , from the frontier point along the normal vector, e_n . The view orientation, ϕ , is the negative direction of the normal vector.

points (Lines 4–6). The position of the current view, \mathbf{x}_c , that captured the new point is stored in X_{cap} for future occlusion handling (Line 7).

If a point in the queue is not a core point then it is (re)classified based on the new measurements (Lines 8–10). Points with insufficient neighbours to be core are (re)classified as frontier points if they have core neighbours or they become outlier points (Lines 11–19). Points with sufficient neighbours are (re)classified as core points (Lines 20–27). If a point has not yet been processed and it is (re)classified as a core point then its neighbours are added to the (re)classification queue and it is marked as processed (Lines 28–31). The classification procedure completes when all new measurements and those in the (re)classification queue are processed.

Classifying sensor measurements based on the density of neighbouring points distinguishes scene regions that are completely observed (i.e., consist only of core points) from those that require additional measurements (i.e., contain frontier and outlier points). The frontier points identified along the boundary between these regions are used to propose views that can improve the observation by extending the coverage of completely observed scene surfaces.

3.3 Proposing Views

Observation coverage is improved by capturing measurements from surfaces around frontier points. Views are proposed to observe the frontiers by estimating the local surface geometry from measurements within the r -radius neighbourhoods. The surface geometry is described by a set of orthogonal vectors computed from an eigendecomposition of the neighbouring measurements (Section 3.3.1). They represent the local surface normal, a boundary between fully and partially observed surfaces and the direction of incomplete observation (i.e., a frontier vector). The outwards facing normal direction is determined by evaluating the visibility of vectors pointing in both potential directions (Section 3.3.2).

Each view, $\mathbf{v} \equiv (\mathbf{x}, \phi)$, is proposed to observe the local surface region around a target frontier point, f (Fig. 5). The view position, \mathbf{x} , is set at the specified view distance, d , along the surface normal. The view orientation, ϕ , is defined by the locally estimated surface normal, e_n , to maximise surface coverage and improve measurement accuracy.

Algorithm 4 ProposeViews($\mathbf{v}_c, P, P', P_f, V, E_{\text{surf}}$)

```

1:  $\mathbf{v}_c \equiv (\mathbf{x}_c, \phi_c)$ ;  $E_{\text{surf}}[\mathbf{f}] \equiv (\mathbf{e}_n, \mathbf{e}_f, \mathbf{e}_b)$ 
2: for all  $\mathbf{f} \in P_f$  and  $V[\mathbf{f}] = \text{NULL}$  do
3:   EstimateSurface( $\mathbf{v}_c, \mathbf{f}, P, P', E_{\text{surf}}$ )
4:    $V[\mathbf{f}] \leftarrow (\mathbf{f} + d\mathbf{e}_n, -\mathbf{e}_n)$ 
5: end for

```

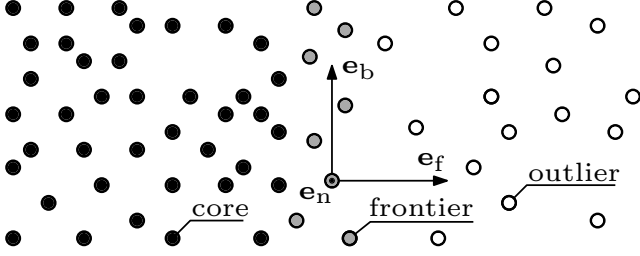


Figure 6. An illustration of the orthogonal vectors that represent the local surface geometry (Alg. 5). The normal vector, \mathbf{e}_n , is normal to the local plane (out of page), the frontier vector, \mathbf{e}_f , points towards the region of partial observation, and the boundary vector, \mathbf{e}_b , lies along the boundary between the fully and partially observed regions.

Algorithm 4 presents the generation of a new view proposal for each new frontier point, \mathbf{f} , without an associated view (Line 2). Measurements within an r -radius of the frontier point are processed, together with the frontier, to estimate the local surface geometry, $E_{\text{surf}}[\mathbf{f}]$ (Line 3; Alg. 5). A new view is then generated and associated with the processed frontier point in the view proposal set, V (Line 4).

3.3.1 Estimating the Surface Geometry The surface geometry around a frontier point is estimated by an eigendecomposition of measurements within an r -radius of the frontier. This produces a planar estimate defined by three orthogonal vectors. Each vector defines one component of the local surface geometry (Fig. 6).

Algorithm 5 presents the estimation of local surface geometry. A planar estimate of the local geometry around a frontier point, \mathbf{f} , is computed from a matrix representation, $\mathbf{D} \in \mathbb{R}^{3 \times |N_f|}$, of its neighbours, N_f (Lines 1–2). A covariance matrix, \mathbf{A} , is computed from the neighbourhood matrix and an eigendecomposition is performed to produce a set of eigenvalues, Λ , and associated eigenvectors, Υ , that satisfy the eigenequation (Lines 3–5).

Each eigenvector describes one component of the estimated surface geometry. The normal vector, \mathbf{e}_n , is orthogonal to the surface plane. The frontier vector, \mathbf{e}_f , lies on the surface plane and points in the direction of partial observation. The boundary vector, \mathbf{e}_b , points along the border between partially and fully observed surfaces. The eigenvectors are assigned based on their eigenvalues.

The normal vector, \mathbf{e}_n , points along the axis associated with the least variation in neighbouring measurements. It is the eigenvector with the minimum eigenvalue (Line 6). The correct direction for the normal vector (i.e., outwards from the surface) is determined by evaluating the visibility of vectors pointing in both potential directions from the current view (Line 7; Alg. 6).

The frontier vector, \mathbf{e}_f , points towards the partially observed region of the scene. It is the remaining eigenvector with the greatest dot product with the mean of the

Algorithm 5 EstimateSurface($\mathbf{v}_c, \mathbf{f}, P, P', E_{\text{surf}}$)

```

1:  $N_f \leftarrow \text{Neighbours}_r(P, r, \mathbf{f}) \cup \{\mathbf{f}\}$ 
2:  $\mathbf{D} \leftarrow [\mathbf{p}_1 - \mathbf{f}, \dots, \mathbf{p}_n - \mathbf{f}]$  where  $\mathbf{p}_i \in N_f$ 
3:  $\mathbf{A} \leftarrow \mathbf{D}\mathbf{D}^T$ 
4:  $\Lambda \leftarrow \text{eigenvalues}(\mathbf{A})$  where  $\Lambda \equiv (\lambda_1, \lambda_2, \lambda_3)$ 
5:  $\Upsilon \leftarrow \text{eigenvectors}(\mathbf{A})$  where  $\Upsilon \equiv (\mathbf{v}_1, \mathbf{v}_2, \mathbf{v}_3)$ 
6:  $\mathbf{e}_n \leftarrow \{\mathbf{v}_i \mid \lambda_i = \min\{\Lambda\}\}$ 
7: DirectNormal( $\mathbf{v}_c, \mathbf{f}, \mathbf{e}_n, P'$ )
8:  $\bar{\mathbf{p}} \leftarrow \frac{1}{|N_f|} \sum_{\mathbf{p} \in N_f} (\mathbf{f} - \mathbf{p})$ 
9:  $\mathbf{e}_f \leftarrow \arg \max_{\mathbf{v}_i \in \Upsilon \setminus \mathbf{e}_n} (|\bar{\mathbf{p}} \cdot \mathbf{v}_i|)$ 
10:  $\mathbf{e}_f \leftarrow \text{sign}(\bar{\mathbf{p}} \cdot \mathbf{e}_f) \mathbf{e}_f$ 
11:  $\mathbf{e}_b \leftarrow \mathbf{e}_n \times \mathbf{e}_f$ 
12:  $E_{\text{surf}}[\mathbf{f}] \leftarrow (\mathbf{e}_n, \mathbf{e}_f, \mathbf{e}_b)$ 

```

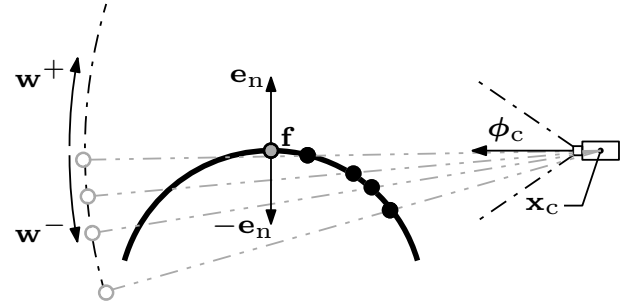


Figure 7. An illustration of how the correct normal direction is determined (Alg. 6). Normal vectors pointing in opposite directions, \mathbf{e}_n and $-\mathbf{e}_n$, have their visibility from the current view, $\mathbf{v}_c \equiv (\mathbf{x}_c, \phi_c)$, evaluated. The correct normal vector will not be occluded by surface measurements closer to the current view (black dots). This vector is found by projecting the occluding measurements onto a sphere and searching along both projected vectors, \mathbf{w}^+ and \mathbf{w}^- , until free space is found.

neighbouring measurements, $\bar{\mathbf{p}}$ (Lines 8–9). The vector direction is defined to have a positive dot product with a vector from the mean point to the frontier to orient it towards the partially observed region of the scene (Line 10).

The boundary vector, \mathbf{e}_b , is locally tangential to the border between the density regions and is defined by the cross product of the normal and frontier vectors (Line 11). The three orthogonal vectors are then stored in E_{surf} (Line 12).

3.3.2 Determining the Correct Normal Direction The views proposed to observe frontier points are defined by the associated surface normals. It is necessary to ensure these normals point outwards from the surface in order to obtain valid views.

The direction of a normal can often be defined as pointing towards the current view. This technique works well when the current view is close to the surface normal but can fail when it observes the surface at an acute angle. In this scenario, the sightline and surface normal are nearly perpendicular and measurement noise can corrupt the identification of the outwards facing normal direction.

A more robust method to determine the outwards facing normal direction is to evaluate the visibility of both potential vectors from the current view (Fig. 7). The normal direction pointing outwards from the surface will not be occluded by measurements while the other direction will be. This method

Algorithm 6 DirectNormal($\mathbf{v}_c, \mathbf{f}, \mathbf{e}_n, P'$)

```

1:  $\mathbf{v}_c \equiv (\mathbf{x}_c, \phi_c)$ 
2:  $\mathbf{w}^+ \leftarrow \mathbf{f} - \mathbf{x}_c$ 
3:  $\mathbf{w}^- \leftarrow \mathbf{w}^+$ 
4: repeat
5:    $\mathbf{w}^+ \leftarrow \mathbf{w}^+ + v\mathbf{e}_n$ 
6:    $\mathbf{w}^- \leftarrow \mathbf{w}^- - v\mathbf{e}_n$ 
7:    $J \leftarrow \left\{ \frac{\mathbf{p} - \mathbf{x}_c}{\|\mathbf{p} - \mathbf{x}_c\|} \mid \mathbf{p} \in P' \wedge \|\mathbf{p} - \mathbf{x}_c\| < \|\mathbf{w}^+\| \right\}$ 
8:    $N_{\mathbf{w}^+} \leftarrow \text{Neighbours}_r \left( J, v, \frac{\mathbf{w}^+}{\|\mathbf{w}^+\|} \right)$ 
9:    $N_{\mathbf{w}^-} \leftarrow \text{Neighbours}_r \left( J, v, \frac{\mathbf{w}^-}{\|\mathbf{w}^-\|} \right)$ 
10: until  $N_{\mathbf{w}^+} = \emptyset$  or  $N_{\mathbf{w}^-} = \emptyset$ 
11: if  $N_{\mathbf{w}^+} \neq \emptyset$  and  $N_{\mathbf{w}^-} = \emptyset$  then
12:    $\mathbf{e}_n \leftarrow -\mathbf{e}_n$ 
13: end if

```

is more robust to sensor noise and the relative orientation of the surface normal to the sight line from the current view.

The visibility of the two potential normal vectors from the current view is evaluated by sampling points along each vector, starting at the frontier point, and checking for an unoccluded sight line. The visibility of points is evaluated in both directions until the first unoccluded point is found and its corresponding vector defines the outwards facing normal direction. It is necessary to evaluate the visibility of multiple points in each direction as noisy measurements may incorrectly occlude points close to the surface.

The visibility of points is evaluated by projecting them onto the surface of a unit sphere centred on the current view, inspired by Hidden Point Removal (HPR; Katz et al. 2007). Measurements obtained from the current view that are closer to the view than the normal vectors are also projected. This projection preserves the relative orientation of points to the view while normalising the distance. Projected points with similar sight lines are close to each other on the sphere surface and a point is considered occluded if projected sensor measurements exist within a specified radius.

Algorithm 6 presents the calculation of the outwards facing normal direction. Sampled points in each vector direction, \mathbf{w}^+ and \mathbf{w}^- , are initialised to the position of the frontier point relative to the current view position, $\mathbf{f} - \mathbf{x}_c$ (Lines 2–3). These sampled points are iteratively moved along the normal vectors until a search for projected measurements on the sphere in either direction returns an empty set (Line 4).

In each iteration, the sampled points are moved along their respective vectors by the visibility search distance, v (Lines 5–6). Newly captured measurements that are closer to the current view position than the sampled points are projected onto the surface of a unit sphere centred on the current view position, \mathbf{x}_c , to create a projected set, J (Line 7). The sampled points are then projected onto the sphere surface and the set of projected measurements is searched to identify any occluding points within an v -radius of the projected samples (Lines 8–9). The outwards facing normal direction is found when either of the search result sets, $N_{\mathbf{w}^+}$ or $N_{\mathbf{w}^-}$, contains no occluding points (Line 10). If the negative normal direction set is empty, $N_{\mathbf{w}^-} = \emptyset$, and the positive set is not then the normal is reversed (Lines 11–13).

Algorithm 7 RefineViews($\mathbf{v}_c, P, P_f, P_o, V, X_{\text{cap}}, E_{\text{surf}}$)

```

1:  $\mathbf{v}_c \equiv (\mathbf{x}_c, \phi_c)$ 
2:  $\mathbf{v}^* \leftarrow \text{NULL}$ 
3:  $N_{\mathbf{v}_c} \leftarrow \text{Neighbours}_k(V, \tau, \mathbf{x}_c)$ 
4: for all  $\mathbf{v} \in N_{\mathbf{v}_c}$  do
5:    $\mathbf{f} \leftarrow \mathbf{f} \in P_f$  s.t.  $\mathbf{v} = V[\mathbf{f}]$ 
6:   if IsOccluded( $\mathbf{v}, \mathbf{f}, P, E_{\text{surf}}$ ) then
7:     OptimiseView( $\mathbf{v}^*, \mathbf{f}, P, X_{\text{cap}}, E_{\text{surf}}$ )
8:     if IsOccluded( $\mathbf{v}^*, \mathbf{f}, P, E_{\text{surf}}$ ) then
9:        $P_f \leftarrow P_f \setminus \mathbf{f}$ 
10:       $P_o \leftarrow P_o \cup \mathbf{f}$ 
11:     else
12:        $V[\mathbf{f}] \leftarrow \mathbf{v}^*$ 
13:     end if
14:   end if
15: end for

```

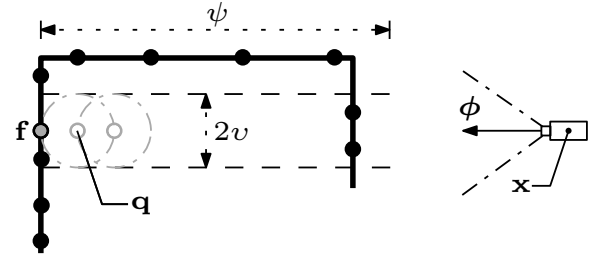


Figure 8. An illustration of detecting occlusions between a frontier point and its associated view (Alg. 8). Measurements (black dots) within a set distance of the sight line are assumed to represent occluding surfaces. They are found by performing an v -radius search around discrete points (grey circles), $\mathbf{q} \in Q$, up to a distance, ψ , from the frontier (grey dot).

This method is able to reliably determine the outwards facing normal direction for the estimated surface around a frontier point. It improves observation efficiency by identifying the correct direction from which to propose a view and reduces the number of failed views attempted.

3.4 Refining Views

Proposed views will only observe the target frontier points when they are not occluded. Occlusions are handled *proactively* by identifying occluded views before they are attempted (Section 3.4.1). These occluded views are refined to alternative unoccluded views (Section 3.4.2).

Algorithm 7 presents the proactive identification of known occlusions and the resulting view refinement. Only the τ -nearest views, $N_{\mathbf{v}_c}$, to the current sensor position, \mathbf{x}_c , are selected from the view proposal set, V , using k -Nearest Neighbours (k -NN; Altman 1992) and processed to maintain a reasonable computational time (Lines 3–5). If occluding measurements are found (Line 6; Alg. 8) then an optimisation strategy is used to identify an alternative unoccluded view of the frontier point (Line 7; Alg. 10). If an unoccluded view is not found the frontier is considered unobservable and reclassified as an outlier (Lines 8–10); otherwise, the existing view is replaced (Lines 11–13).

3.4.1 Detecting Occlusions A frontier point is considered occluded if measurements exist within the visibility search distance, v , of the sight line of the proposed view. Occluding measurements are found by searching the v -radius neighbourhoods of points sampled along the sight

Algorithm 8 IsOccluded($\mathbf{v}, \mathbf{f}, P, E_{\text{surf}}$)

```

1:  $\mathbf{v} \equiv (\mathbf{x}, \phi)$ 
2:  $\zeta \leftarrow 0$ 
3: GetVisibilityOffset( $\mathbf{f}, \zeta, P, E_{\text{surf}}$ )
4:  $\phi_s = \frac{\mathbf{f} - \mathbf{x}}{\|\mathbf{f} - \mathbf{x}\|}$ 
5:  $Q \leftarrow \{\mathbf{f} - i\phi_s \mid i = \zeta, \zeta + v, \dots, \psi\}$ 
6:  $N_q \leftarrow \bigcup_{\mathbf{q} \in Q} \text{Neighbours}_r(P, v, \mathbf{q})$ 
7: return  $N_q \neq \emptyset$ 

```

Algorithm 9 GetVisibilityOffset($\mathbf{f}, \zeta, P, E_{\text{surf}}$)

```

1:  $E_{\text{surf}}[\mathbf{f}] \equiv (\mathbf{e}_n, \mathbf{e}_f, \mathbf{e}_b)$ 
2: repeat
3:    $\zeta \leftarrow \zeta + v$ 
4:    $\mathbf{q} \leftarrow \mathbf{f} + \zeta \mathbf{e}_n$ 
5:    $N_q \leftarrow \text{Neighbours}_r(P, v, \mathbf{q})$ 
6: until  $N_q = \emptyset$  or  $\zeta \geq \psi$ 

```

line (Fig. 8). A frontier is visible from a view if occluding measurements are not found around any sampled points.

Algorithm 8 presents occlusion detection between a frontier point and a view. Points are sampled along the sight line at an v -interval, starting at an offset from the frontier, ζ , and ending at the occlusion search distance, ψ (Lines 3–5). The v -radius neighbourhood around every sampled point is searched for occluding measurements (Line 6). The view is occluded if the union of the search result sets, N_q , is not empty (Line 7).

The search for occluding measurements starts at an offset from the frontier to account for measurement noise. A suitable offset is identified by searching along the local surface normal until the first region of free space is found.

Algorithm 9 presents the calculation of this offset. Points are incrementally sampled along the normal vector at an v -interval, starting at the frontier point, until the v -radius neighbourhood around the newest sampled point is empty or the occlusion search distance is reached (Lines 2–6).

Proactively detecting known occlusions improves observation efficiency by reducing the number of unsuccessful views. This method is also used to quantify the shared visibility of frontiers between views, which helps select next best views that observe more frontiers.

3.4.2 Proposing an Unoccluded View Occluded views are updated to an unoccluded view by finding the sight line to their frontier point that has the greatest separation from any occluding measurements. This sight line provides visibility of surrounding surfaces and the best chance that the frontier will be successfully observed.

A frontier point is likely occluded when there are measurements between it and the proposed viewing position. A frontier's visibility from different viewing positions can be found by projecting possibly occluding measurements onto a unit sphere (Fig. 9). The sphere centre may be slightly offset from the frontier to account for noisy measurements. The projection preserves the direction of occluding measurements while placing them on a uniform manifold for efficient processing and is inspired by HPR (Katz et al. 2007).

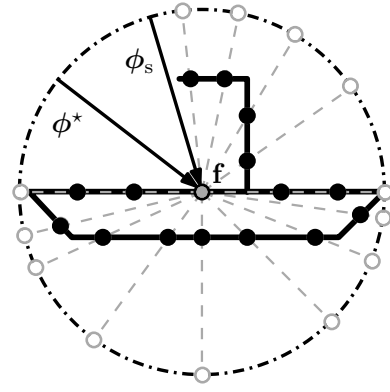


Figure 9. A 2D illustration of the spherical projection used to find an unoccluded sight line of a target frontier point (grey dot), \mathbf{f} (Alg. 10). Measurements (black dots) are projected onto a unit sphere (grey circles) centred on the frontier point. The optimally unoccluded view orientation, ϕ^* , is maximally separated from the projected points. The sight line from the capturing view, ϕ_s , is known to be unoccluded.

A safely unoccluded view of the frontier point is found by solving a *maximin* optimisation problem on the spherical projection. This maximises the minimum distance between the viewing direction and any of the projected occluding measurements. The maximin problem solution is the antipole (Drezner and Wesolowsky 1983) of the complementary *minimax* problem solution (Patel and Chidambaram 2002).

The minimax solution is the centre of the smallest spherical cap that contains the projected points. This cap is defined by a plane intersecting the sphere and is found by optimising the plane normal and its distance from the sphere centre. The minimax solution is the intersection point of the plane normal with the sphere.

The specific optimisation method depends on the distribution of the projected points. If they are spread over more than a hemisphere then the smallest containing cap is found by minimising the distance of the plane from the sphere centre. If the projected points lie on less than a hemisphere then the smallest containing cap is found by maximising the distance of the plane from the sphere centre.

Algorithm 10 presents the calculation of an unoccluded view using this maximin optimisation strategy. The projection centre of the sphere, \mathbf{c} , is offset from the frontier point, \mathbf{f} , by the visibility offset (Alg. 9), ζ , towards the capturing view position, $X_{\text{cap}}[\mathbf{f}]$, as this sight line is known to be unoccluded (Lines 2–4). The neighbouring measurements within the occlusion search distance, ψ , of the frontier are projected onto a unit sphere (Line 5). The projected points, J , are initially assumed to be distributed over more than a hemisphere and the full sphere optimisation is performed (Line 6). The distance of a plane intersecting the sphere from its centre is minimised while ensuring the plane normal satisfies the optimisation constraints and the projected points all lie on the same side of the plane. The plane normal is initialised to the opposite direction of the sight line from the capturing view, ϕ_s , as this is known to be unoccluded. The optimised view orientation, ϕ^* , points in the opposite direction of the optimised normal so that the sphere is intersected at the maximin solution (Line 8).

Algorithm 10 OptimiseView($\mathbf{v}^*, \mathbf{f}, P, X_{\text{cap}}, E_{\text{surf}}$)

```

1:  $\zeta \leftarrow 0$ 
2: GetVisibilityOffset( $\mathbf{f}, \zeta, P, E_{\text{surf}}$ )
3:  $\phi_s \leftarrow \frac{\mathbf{f} - X_{\text{cap}}[\mathbf{f}]}{\|\mathbf{f} - X_{\text{cap}}[\mathbf{f}]\|}$ 
4:  $\mathbf{c} \leftarrow \mathbf{f} - \zeta \phi_s$ 
5:  $J \leftarrow \left\{ \frac{\mathbf{p} - \mathbf{c}}{\|\mathbf{p} - \mathbf{c}\|} \mid \mathbf{p} \in \text{Neighbours}_r(P, \psi, \mathbf{f}) \right\}$ 
   ( $\mathbf{n}^*, e^*$ )  $\leftarrow \arg \min_{\mathbf{n} \in \mathbb{R}^3, e \in [0,1]} e$ 
6:   subject to  $e \leq \mathbf{n}^T \mathbf{n},$ 
                $e \geq \mathbf{n}^T \mathbf{j}, \quad \forall \mathbf{j} \in J,$ 
               initial condition  $\mathbf{n}(0) = -\phi_s$ 
7: if  $e^* \neq 0$  then
8:    $\phi^* \leftarrow -\frac{\mathbf{n}^*}{\|\mathbf{n}^*\|}$ 
9: else
   ( $\mathbf{n}^*, e^*$ )  $\leftarrow \arg \max_{\mathbf{n} \in \mathbb{R}^3, e \in [0,1]} e$ 
10:  subject to  $e \geq \mathbf{n}^T \mathbf{n},$ 
               $e \leq \mathbf{n}^T \mathbf{j}, \quad \forall \mathbf{j} \in J,$ 
              initial condition  $\mathbf{n}(0) = \phi_s$ 
11:   $\phi^* \leftarrow \frac{\mathbf{n}^*}{\|\mathbf{n}^*\|}$ 
12: end if
13:  $\mathbf{x}^* \leftarrow \mathbf{f} - d\phi^*$ 
14:  $\mathbf{v}^* \leftarrow (\mathbf{x}^*, \phi^*)$ 

```

If the projected points lie on less than a hemisphere then the full sphere optimisation converges to a plane bisecting the sphere (i.e., $e^* = 0$) and a hemispherical optimisation is performed (Lines 9–10). The distance of a plane intersecting the sphere from its centre is maximised while ensuring the plane normal satisfies the optimisation constraints and the projected points all lie on the same side of the plane. The plane normal is initialised to the direction of the capturing view orientation as this is known to be unoccluded. The optimised view orientation points in the same direction as the optimised normal (Line 11). After the view optimisation is complete the optimised view position, \mathbf{x}^* , is set at the view distance, d , from the frontier in the opposite direction of the optimised view orientation and the optimised view proposal, \mathbf{v}^* , is set (Lines 13–14).

This optimisation is guaranteed to find a view of a frontier point that is free from known occlusions if one exists. Refining proposed views with it improves the efficiency of scene observations by increasing the chance that a frontier point will be successfully observed. Further efficiency improvements are achieved by quantifying the shared visibility of frontiers between proposed views.

3.5 Quantifying Views

The best views are those that capture the most new surface coverage. SEE quantifies the predicted coverage from a proposed view as the number of visible frontier points. The visibility of frontiers from different views is encoded in a directed *frontier visibility graph* that connects each frontier to the views from which it can be observed. It is used to select

Algorithm 11 GraphViews($\mathbf{v}_c, P_f, V, \mathcal{G}$)

```

1:  $\mathcal{G} \equiv (M, K)$ ;  $\mathbf{m} \equiv (\mathbf{f}, \mathbf{v})$ ;  $\mathbf{v}_c \equiv (\mathbf{x}_c, \phi_c)$ ;  $\mathbf{v}_i \equiv (\mathbf{x}_i, \phi_i)$ 
2:  $M' \leftarrow \{(\mathbf{f}, V[\mathbf{f}]) \mid \mathbf{f} \in P_f\}$ 
3:  $K' \leftarrow K \setminus \{(\mathbf{m}_a, \mathbf{m}_b) \mid \mathbf{f}_a \notin P_f \vee \mathbf{f}_b \notin P_f\}$ 
4:  $N_{\mathbf{v}_c} \leftarrow \text{Neighbours}_k(V, \tau, \mathbf{x}_c)$ 
5: for all  $\mathbf{v}_i \in N_{\mathbf{v}_c}$  do
6:    $\mathbf{f}_i \leftarrow \mathbf{f}_i \in P_f$  s.t.  $\mathbf{v}_i = V[\mathbf{f}_i]$ 
7:    $K' \leftarrow K' \setminus \{(\mathbf{m}_a, \mathbf{m}_b) \mid \mathbf{f}_a = \mathbf{f}_i\}$ 
8:    $N_{\mathbf{v}_i} \leftarrow \text{Neighbours}_k(V, \tau, \mathbf{x}_i)$ 
9:   for all  $\mathbf{v}_j \in N_{\mathbf{v}_i}$  do
10:     $\mathbf{f}_j \leftarrow \mathbf{f}_j \in P_f$  s.t.  $\mathbf{v}_j = V[\mathbf{f}_j]$ 
11:    if  $\neg \text{IsOccluded}(\mathbf{f}_j, \mathbf{v}_i, \psi, v)$  then
12:       $K' \leftarrow K' \cup \{(\mathbf{m}_i, \mathbf{m}_j)\}$ 
13:    end if
14:  end for
15: end for
16:  $\mathcal{G} = (M', K')$ 

```

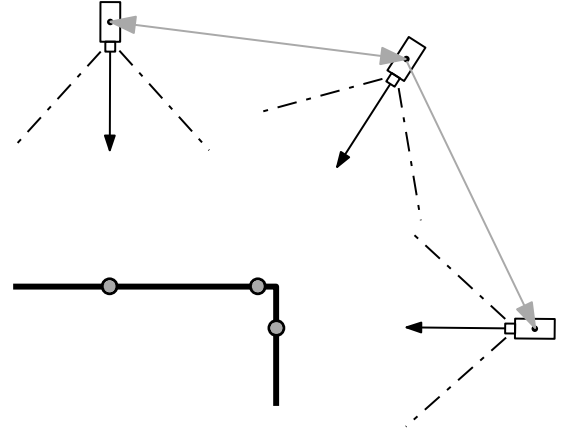


Figure 10. An illustration of the frontier visibility graph (Alg. 11). The connectivity between frontier-view pairs (grey dots and sensors) is represented with directed edges (grey arrows). An edge from a parent to a child denotes that the child frontier point is visible from the parent view proposal.

next best views that can obtain large increases in surface coverage.

The frontier visibility graph, $\mathcal{G} := (M, K)$, represents the view proposals and their visible frontier points (Fig. 10). The graph vertices, M , are pairs, $\mathbf{m} \equiv (\mathbf{f}, \mathbf{v})$, of a frontier point, \mathbf{f} , and its associated view, \mathbf{v} . An edge, $(\mathbf{m}_i, \mathbf{m}_j) \in K$, exists from a parent vertex, \mathbf{m}_i , to a child vertex, \mathbf{m}_j , if the parent view, \mathbf{v}_i , can observe the child frontier point, \mathbf{f}_j . This covisibility is calculated using occlusion detection (Section 3.4.1) and quantifies the expected number of frontiers visible from each view.

Algorithm 11 presents the calculation of the frontier visibility graph. The vertices, M' , are a new set of frontier-view pairs created from the view proposal set, V (Line 2). A new edge set, K' , is created from the existing edge set, K , by removing edges between vertices that have been reclassified as core points (Line 3). Only the set of frontier-view pairs corresponding with the τ -nearest view proposals, $N_{\mathbf{v}_c}$, to the current sensor position, \mathbf{x}_c , are processed in order to reduce the computational cost (Line 4).

Each frontier-view pair, $\mathbf{m}_i = (\mathbf{f}_i, \mathbf{v}_i)$, is processed by removing existing outgoing edges from the graph and adding new outgoing edges to the visible frontier points associated with the τ -nearest view proposals, $N_{\mathbf{v}_i}$ (Lines

Algorithm 12 SelectNBV($\mathbf{v}_c, \mathbf{f}_c, \mathcal{G}$)

```

1:  $\mathcal{G} \equiv (M, K)$ ;  $\mathbf{m} \equiv (\mathbf{f}, \mathbf{v})$ ;  $\mathbf{v} \equiv (\mathbf{x}, \phi)$ ;  $\mathbf{v}_c \equiv (\mathbf{x}_c, \phi_c)$ 
2:  $\mathbf{m}' \leftarrow \arg \min_{\mathbf{m} \in M} (||\mathbf{x} - \mathbf{x}_c||)$ 
3:  $M' \leftarrow \{\mathbf{m} \in M \mid (\mathbf{m}, \mathbf{m}') \in K \wedge \deg^+(\mathbf{m}) > \deg^+(\mathbf{m}')\}$ 
4:  $\mathbf{m}^* \leftarrow \arg \max_{\mathbf{m} \in M'} \left( \frac{\deg^+(\mathbf{m})}{||\mathbf{x} - \mathbf{x}_c||} \right)$ 
5: if  $\mathbf{m}^* = \text{NULL}$  then
6:    $\mathbf{m}^* \leftarrow \mathbf{m}'$ 
7: end if
8:  $(\mathbf{f}_c, \mathbf{v}_c) \leftarrow \mathbf{m}^*$ 

```

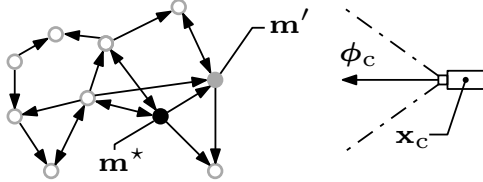


Figure 11. An illustration of the next best view selection metric (Alg. 12). Vertices (grey circles) in the frontier visibility graph represent frontier-view pairs and are connected with directed edges denoting visibility (black arrows). The sensor represents the current view, $\mathbf{v}_c \equiv (\mathbf{x}_c, \phi_c)$. The next best view is the vertex (black dot), \mathbf{m}^* , that has the greatest outdegree relative to its view proposal's distance from the current sensor position, \mathbf{x}_c , with an edge to the vertex (grey dot), \mathbf{m}' , whose view is closest to the sensor.

5–10). The visibility of these frontier points is evaluated using the occlusion detection method (Line 11; Alg. 8). An outgoing edge is added from the processed vertex, \mathbf{m}_i , to the associated vertex, \mathbf{m}_j , if its frontier is visible (Line 12). The new frontier visibility graph is the new vertex and edge sets when all of the queued frontier-view pairs have been processed (Line 16).

The frontier visibility graph quantifies views that should obtain large increases in surface coverage. This information is used by the next best view selection metric to choose views that can capture an efficient scene observation.

3.6 Selecting a Next Best View

Next best views are selected to improve a scene observation while reducing the associated cost. SEE selects a view with the most visible frontier points relative to its distance from the current sensor position. This ratio penalizes views far from the current sensor position that can not observe more frontiers than closer views.

This greedy view selection behaviour may select a distant view with many visible frontier points that then requires the sensor to return to capture closer surfaces. This problem is avoided by requiring the chosen view to have visibility of the frontier point associated with the closest view proposal (Fig. 11). The closest view can have a very small travel distance so it is only selected when it has visibility of at least as many frontiers as any other potential view.

Algorithm 12 presents the selection of next best views. The closest view proposal, \mathbf{m}' , to the current sensor position, \mathbf{x}_c , is used to define the set of permissible views (Lines 2–3). The vertex with the greatest ratio between the number of outgoing edges (i.e., its outdegree) and the distance of its view proposal from the current sensor position, \mathbf{m}^* , is

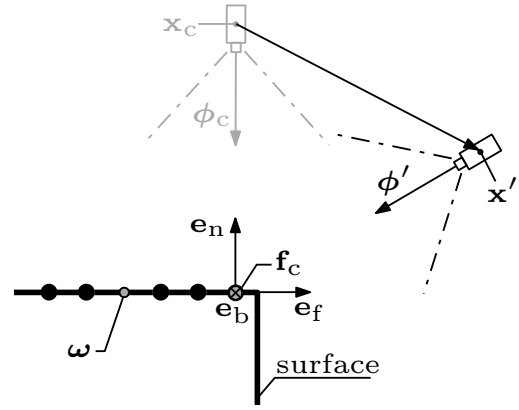


Figure 12. An illustration of a view adjustment around a surface discontinuity (Alg. 13). The frontier point, \mathbf{f}_c , on one side of a surface edge can not be successfully observed by the current view, $\mathbf{v}_c \equiv (\mathbf{x}_c, \phi_c)$. An adjusted view, $\mathbf{v}' \equiv (\mathbf{x}', \phi')$, with visibility around this discontinuity is calculated from the difference between the frontier and the mean (grey dot) of the measurements (black dots) captured from the current view, ω .

chosen as the next view (Line 4). If no such view exists the closest view is selected (Lines 5–7). The next target view and frontier point are then updated to the chosen next best view (Line 8).

This next best view selection metric chooses views that can capture significant improvements in scene coverage while travelling short distances. It enables SEE to obtain complete observations using a low overall travel distance by capturing local surfaces before travelling to observe larger unobserved regions.

3.7 Handling Failed Views

Selected views do not always observe their target frontier points successfully. A view is considered failed when its new measurements do not make its associated frontier point a core point. This occurs when the entire local surface is not visible, either due to occlusions or surface discontinuities (e.g., corners). These failed views must be adjusted to successfully observe their target frontiers.

A new view is proposed by adjusting the failed view based on the captured measurements. The view adjustment shifts a failed view to avoid occlusions and surface discontinuities. This adjustment reduces the separation between the frontier point and the mean of the captured measurements. It is calculated from translations along, and rotations around, the vectors representing the local surface geometry (Fig. 12).

The view adjustment is repeated until the target frontier is successfully observed or a termination criterion is reached. When the separation between the frontier point and the mean of the captured measurements stops decreasing the adjusted view is reinitialized to the viewing position that first captured the frontier as this is known to be unoccluded. This new view is again adjusted until the frontier is successfully observed or the process is terminated. If this process fails too, then the frontier is assumed to be unobservable and it is reclassified as an outlier.

Algorithm 13 presents the view adjustment procedure. The adjustment parameters are initialised if this is the first time the frontier point has been adjusted (Lines 3–7).

Algorithm 13 AdjustView($\mathbf{v}_c, \mathbf{f}_c, P', P_f, P_o, V, X_{\text{cap}}, E_{\text{surf}}$)

```

1:  $\mathbf{v}_c \equiv (\mathbf{x}_c, \phi_c)$ ;  $\mathbf{v}' \equiv (\mathbf{x}', \phi')$ 
2:  $E_{\text{surf}}[\mathbf{f}_c] \equiv (\mathbf{e}_n, \mathbf{e}_f, \mathbf{e}_b)$ ;  $\mathbf{s} \equiv [s_0, s_1, s_2]^T$ 
3: if  $D[\mathbf{f}_c] = \text{NULL}$  then
4:    $D[\mathbf{f}_c] \leftarrow \infty$ 
5:    $A[\mathbf{f}_c] \leftarrow 1$ 
6:    $V_{\text{switch}}[\mathbf{f}_c] \leftarrow \text{FALSE}$ 
7: end if
8:  $\mathbf{C} \leftarrow [\mathbf{e}_n \ \mathbf{e}_f \ \mathbf{e}_b]$ 
9:  $\omega \leftarrow \frac{1}{|P'|} \sum_{\mathbf{p} \in P'} \mathbf{p}$ 
10:  $\mathbf{s} \leftarrow \mathbf{C}^T(\mathbf{f}_c - \omega)$ 
11: if  $\|\mathbf{s}\| < D[\mathbf{f}_c]$  then
12:    $\mathbf{t}_f \leftarrow (A[\mathbf{f}_c] + 1)s_1\mathbf{e}_f$ 
13:    $\mathbf{t}_b \leftarrow (A[\mathbf{f}_c] + 1)s_2\mathbf{e}_b$ 
14:    $\theta_b = \tan^{-1} \left( \frac{dA[\mathbf{f}_c]s_1}{d^2 + (A[\mathbf{f}_c] + 1)s_1^2} \right)$ 
15:    $\theta_f = \tan^{-1} \left( \frac{dA[\mathbf{f}_c]s_2}{d^2 + (A[\mathbf{f}_c] + 1)s_2^2} \right)$ 
16:    $\mathbf{R}_b \leftarrow \mathbf{I} + (\sin \theta_b)\mathbf{e}_b^\times + (1 - \cos \theta_b)(\mathbf{e}_b^\times)^2$ 
17:    $\mathbf{R}_f \leftarrow \mathbf{I} + (\sin \theta_f)\mathbf{e}_f^\times + (1 - \cos \theta_f)(\mathbf{e}_f^\times)^2$ 
18:    $\phi' \leftarrow \phi_c - (\mathbf{R}_f(\mathbf{t}_b + \mathbf{R}_b(\mathbf{t}_f + \mathbf{x}_c))$ 
19:    $D[\mathbf{f}_c] \leftarrow \|\mathbf{s}\|$ 
20:    $A[\mathbf{f}_c] \leftarrow 2A[\mathbf{f}_c]$ 
21: else if  $\neg V_{\text{switch}}[\mathbf{f}_c]$  then
22:    $\phi' \leftarrow \phi_c - X_{\text{cap}}[\mathbf{f}_c]$ 
23:    $D[\mathbf{f}_c] \leftarrow \infty$ 
24:    $A[\mathbf{f}_c] \leftarrow 1$ 
25:    $V_{\text{switch}}[\mathbf{f}_c] \leftarrow \text{TRUE}$ 
26: else
27:    $P_f \leftarrow P_f \setminus \mathbf{f}_c$ 
28:    $P_o \leftarrow P_o \cup \mathbf{f}_c$ 
29: end if
30: if  $\mathbf{f}_c \in P_f$  then
31:    $\mathbf{x}' \leftarrow \mathbf{f}_c - d \frac{\phi'}{\|\phi'\|}$ 
32:    $V[\mathbf{f}_c] \leftarrow \mathbf{v}'$ 
33: end if

```

Individual adjustments are calculated using a scaling factor, $A[\mathbf{f}_c]$, that increases with each subsequent adjustment. A view proposal is adjusted if the current separation distance between the frontier position and the mean of the captured measurements is less than the previous separation distance, $D[\mathbf{f}_c]$. The view switch flag, $V_{\text{switch}}[\mathbf{f}_c]$, indicates when the adjustment of a view proposal has failed and the view has been reset to the frontier's capturing view position.

The view adjustment is performed in a coordinate frame, \mathbf{C} , defined by the local surface geometry (Lines 8–9). The current separation distance, $\mathbf{s} = [s_0, s_1, s_2]^T$, between the frontier, \mathbf{f}_c , and the mean of the captured measurements, ω , is calculated and the view is only adjusted if it is less than the previous separation distance (Lines 10–11).

The translational adjustments, \mathbf{t}_f and \mathbf{t}_b , along each axis, \mathbf{e}_f and \mathbf{e}_b , are the scaled separation distances (Lines 12–13). They move the centre of the viewing frustum towards the regions where the previous view captured no measurements. This moves the view around discontinuities at the intersection of different surfaces (i.e., corners).

The rotational adjustments, \mathbf{R}_b and \mathbf{R}_f , for each axis are computed by Rodrigues' rotation formula (Rodrigues 1840),

$$\mathbf{R} = \mathbf{I} + (\sin \theta)\mathbf{u}^\times + (1 - \cos \theta)(\mathbf{u}^\times)^2,$$

where \mathbf{I} is the identity matrix, θ is the angle of rotation, \mathbf{u} is the axis of rotation, and $(\cdot)^\times$ is the skew symmetric matrix of a vector,

$$\begin{bmatrix} u_0 \\ u_1 \\ u_2 \end{bmatrix}^\times = \begin{bmatrix} 0 & -u_2 & u_1 \\ u_2 & 0 & -u_0 \\ -u_1 & u_0 & 0 \end{bmatrix}.$$

These rotations move the view both around newly discovered occlusions and towards the unobserved side of surface discontinuities (Lines 14–17).

The adjusted view orientation, ϕ' , is the vector pointing towards the frontier point from the newly translated and rotated view position (Line 18). The separation distance parameter is updated in case further adjustments are required (Line 19). The adjustment scaling factor is doubled to prevent the magnitude of future adjustments from converging to zero as the separation distance decreases (Line 20).

A view adjustment is terminated when the separation distance stops decreasing. If the adjustment started from the initial view proposal then the new view orientation, ϕ' , is the sight line from the frontier's capturing view, as this is known to be occlusion-free (Lines 21–22). The adjustment parameters are reinitialised as this *switched* view is also adjusted reactively if it is unsuccessful (Lines 23–25). If adjustment of the switched view proposal also fails then the frontier point is considered unobservable and it is reclassified as an outlier (Lines 26–29).

The new position, \mathbf{x}' , of an adjusted or switched view is set along the new view direction at the specified view distance (Line 30–31). The new view, \mathbf{v}' , then replaces the existing one in the set of view proposals (Line 32).

This reactive adjustment of failed views enables scene coverage to be extended beyond surface discontinuities and behind previously unseen occluding surfaces. It helps SEE obtain highly complete observations by capturing measurements from surfaces with restricted visibility that would otherwise be unobservable.

3.8 Completing an Observation

A scene observation completes when there are no remaining frontiers and all measurements are classified as either core or outlier points. The extent of a scene observation can be bounded by discarding all points outside of a given volume.

4 Simulation Experiments

SEE is compared with seven volumetric NBV planning approaches: Average Entropy (AE; Kriegel et al. 2015), Area Factor (AF; Vasquez-Gomez et al. 2014), Occlusion Aware (OA; Delmerico et al. 2018), Proximity Count (PC; Delmerico et al. 2018), Rear Side Entropy (RSE; Delmerico et al. 2018), Rear Side Voxel (RSV; Delmerico et al. 2018) and Unobserved Voxel (UV; Delmerico et al. 2018). The implementations of these volumetric approaches are provided by Delmerico et al. (2018).

Experiments were performed with six small-scale models: Newell Teapot (Newell 1976), Stanford Bunny (Turk and Levoy 1994), Stanford Dragon (Curless and Levoy 1996), Stanford Armadillo (Krishnamurthy and Levoy 1996), Happy Buddha (Curless and Levoy 1996) and Helix

Table 2. The field-of-view in degrees, θ_x and θ_y , and resolution in pixels, w_x and w_y , of the RGB-D camera and LiDAR used to capture sensor measurements in the experiments in Section 4.

Property	RGB-D Camera	Rotating LiDAR	Units
θ_x	70	60	degrees
θ_y	43	40	degrees
w_x	848	1200	pixels
w_y	480	800	pixels

(Burkardt 2012), and three large-scale models: Statue of Liberty (Fisher 2015), Radcliffe Camera (Boronczyk 2016) and Notre-Dame de Paris (FabShop 2015). The algorithms were run for 100 independent experiments on each model.

The small models were observed in a robot arm simulation environment. This consisted of a UR10 robot arm with an RGB-D camera attached to the end effector and a turntable (Fig. 13). The turntable centre and UR10 base are separated by 0.75 m. The turntable has a diameter of 0.8 m, so the small models are scaled to fit within a 0.8x0.8x0.6 m bounding box. The maximum model height is 0.6 m so that views above a model are reachable by the end effector.

The large models were observed in an aerial simulation environment. Measurements are captured by a LiDAR mounted onto the underside of a quadrotor with a two-axis gimbal. The large models are placed at the origin on a virtual ground plane and scaled to fit within a 40x40x40 m box. The quadrotor is able to reach any collision-free view position and the two-axis gimbal can position the LiDAR at any view orientation in the hemisphere below the quadrotor.

The simulated sensors are defined by a field-of-view in degrees, θ_x and θ_y , and a resolution in pixels, w_x and w_y (Table 2). Sensor measurements were obtained by raycasting into the triangulated surface of a model and adding Gaussian noise ($\mu = 0$ m, $\sigma = 0.01$ m) to the ray intersections.

Collision-free paths between views are planned with Adaptively Informed Trees (AIT*; Strub and Gammell 2020, 2022), using the Open Motion Planning Library (OMPL; Sucas et al. 2012), and executed with MoveIt (Coleman et al. 2014). The platform-specific reachability of each next best view is evaluated before planning a path and any unreachable view is adjusted to a reachable view based on platform-specific constraints. If the path planning to a view fails then the NBV algorithm is forced to select a different view.

SEE selects next best views until its completion criterion is satisfied. The volumetric approaches use a view limit termination criterion that must be set by the user. For each model, the volumetric algorithms are limited to the largest number of views taken by SEE for any run on the model.

View proposals for the volumetric approaches are sampled from a surface encompassing the scene, in this case a hemisphere, as presented by Vasquez-Gomez et al. (2014) and Delmerico et al. (2018). Kriegel et al. (2015) does not sample views from an encompassing view surface but we use the implementation provided by Delmerico et al. (2018) which does. The radius of the view hemisphere is set to the sum of the view distance, d , and a surface offset equal to the mean distance of points in the model from the origin. The number of views sampled from the hemisphere is 2.4 times the view limit, as presented by Delmerico et al. (2018).

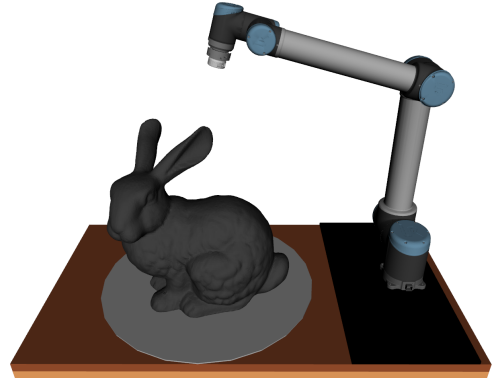


Figure 13. The UR10 simulation environment used in the experiments in Section 4. An object (dark grey) is placed on the turntable (light grey) and measurements are captured with an RGB-D camera attached to the UR10 end effector.

4.1 Performance Metrics

The observation performance of each approach is quantified by the surface coverage obtained, travel distance required and computation time used when capturing an observation. These values are averaged across the 100 independent experiments performed on each model with each approach.

The surface coverage is calculated from the mesh vertices of the 3D model, S . A model vertex is considered covered when the captured pointcloud has a measurement within a user-selected registration radius, η (Table 3). The surface coverage obtained by an algorithm is then measured as the ratio of covered model points,

$$S_{\text{reg}} = \{s \in S \mid \exists p \in P, \|s - p\| \leq \eta\},$$

to total model points,

$$\text{Coverage} = \frac{|S_{\text{reg}}|}{|S|}.$$

The sensor travel distance is measured as the summed lengths of the paths travelled by the sensor between views. The total observation time is measured as the sum of NBV planning, path planning, and movement times for each view. NBV planning time is the computation time to process new sensor measurements and select a next best view and does not include the cost of simulating measurements. The path planning time is the computation time to plan a collision-free path between views. The movement time is the time to move the sensor from its current position to the next best view.

4.2 Algorithm Parameters

Table 3 presents the parameters used by SEE and the evaluated volumetric approaches to observe the small- and large-scale scene models. The minimum separation distance between sensor measurements used by SEE, ϵ , is also applied to the volumetric approaches to reduce memory consumption and computational cost for all the evaluated approaches and ensure a fair comparison.

4.2.1 Small Models The target measurement density, ρ , for SEE on the small models is computed from the resolution radius, view distance and sensor properties (Alg. 2, Line 4). The resolution radius, r , is set large enough to robustly

Table 3. The parameters used for SEE, the volumetric approaches and the associated analysis in the experiments in Section 4. Values in *italics* were derived from other parameters.

	Small Models	Large Models	Units
ρ	490738	300	points per m ³
r	0.03	0.15	m
d	0.5	35.6	m
ϵ	0.003	0.06	m
ψ	0.5	20	m
v	0.01	0.15	m
τ	100	100	number of views
ξ	0.1	0.01	
γ	0	0	
η	0.005	0.05	m

handle measurement noise and is also used as the voxel size for the volumetric approaches. The view distance, d , is chosen to be far enough that a significant proportion of the scene is visible from each view while remaining reachable by the UR10. The occlusion search distance, ψ , is set equal to the view distance so that all known occlusions can be identified. The visibility search distance, v , is set slightly smaller than the resolution radius so that frontier points on narrow concave surfaces can be accurately evaluated. The view update limit, τ , is chosen to process a large number of proposed views while maintaining a reasonable computational cost. The values of these parameters are presented in Table 3.

The raycasting resolution parameter, ξ , sets the fraction of the sensor resolution that is raycast by volumetric approaches to calculate the IG value of view proposals. It is chosen to be sufficiently small to attain a reasonable computational time without reducing the observation performance. The travel cost weight, γ , for the volumetric approaches is set to zero so that they obtain the highest surface coverage possible within the specified view limit.

4.2.2 Large Models The target density for SEE on the large models is set to capture small surface details. The resolution radius is chosen to be large enough to accurately estimate the local surface geometry and is again also used as the voxel size for the volumetric approaches. The view distance is computed from these parameters and the sensor properties (Alg. 2, Line 6). The occlusion search distance is set to half the model size to reduce the computational cost. The visibility search distance is set to the resolution radius. The view update limit is set as large as possible while maintaining a reasonable computational cost. The values of these parameters are presented in Table 3.

The raycasting resolution for the volumetric approaches is chosen to attain a feasible computational cost for observing the large models. Their travel cost weight is again set to zero for the highest surface coverage.

4.3 Discussion

The results (Figs. 14–16) show that an unstructured measurement-direct NBV planning approach captures highly complete scene observations with greater efficiency than structured volumetric approaches. SEE achieves similar or better surface coverage than the volumetric approaches on

every tested model while using fewer views, shorter travel distances and less observation time. It captures greater surface coverage per unit of travel distance on every model, which clearly demonstrates the benefit of selecting next best views that can obtain significant improvements in surface coverage while moving short distances. It captures higher coverage per unit of computation time on most models, except for those with complex self-occlusions, as unlike the volumetric approaches SEE does not require computationally expensive raycasting to evaluate potential views. SEE does spend extra computational effort evaluating the visibility of nearby views and avoiding occlusions, but the resulting improvement in view selection reduces the net computational time by requiring fewer views. The following sections discuss the performance of SEE on individual small (Section 4.3.1) and large (Section 4.3.2) models, and review limitations of the volumetric approaches (Section 4.3.3).

4.3.1 Small Models SEE captures similar or better surface coverage than all of the tested volumetric approaches on every small model using fewer views, less travel distance and a shorter observation time. It also attains greater surface coverage per unit of travel distance than all of the volumetric approaches on every model.

SEE obtains higher surface coverage than all of the volumetric approaches on every small model except for the Newell Teapot. It achieves marginally lower surface coverage on the Newell Teapot but requires fewer views, a shorter travel distance and less observation time to do so. This is because sensor noise causes the intersections between the teapot body and the spout/handle to be prematurely classified as fully observed.

SEE achieves greater surface coverage per unit of computational time than all of the volumetric approaches on every small model except for the Stanford Armadillo and Helix, where it slightly underperforms the RSV volumetric approach. On both of these models SEE took similar NBV planning time but more path planning time than RSV. This was a result of difficult-to-reach views that observed the undersides of the arms and torso for the Armadillo and the interior surfaces of the spiral for the Helix.

4.3.2 Large Models SEE obtains similar or greater surface coverage than all of the evaluated volumetric approaches on every large model using less views, shorter travel distances and a lower observation time. It also attains higher surface coverage per unit of travel distance than all of the volumetric approaches on every model.

SEE achieves higher surface coverage overall, and greater surface coverage per unit of computation time, than all of the volumetric approaches on every large model except for the Notre-Dame de Paris, where it performs marginally worse than all of the volumetric approaches except PC. This is because it took SEE more planning time to adjust views for significant occlusions caused by the flying buttresses without successfully increasing surface coverage underneath these uniquely challenging features; however, SEE still observes the Notre-Dame de Paris using fewer views, a significantly shorter travel distance and a far lower observation time than all of the volumetric approaches.

4.3.3 Volumetric Limitations The results demonstrate that the final surface coverage of the volumetric approaches

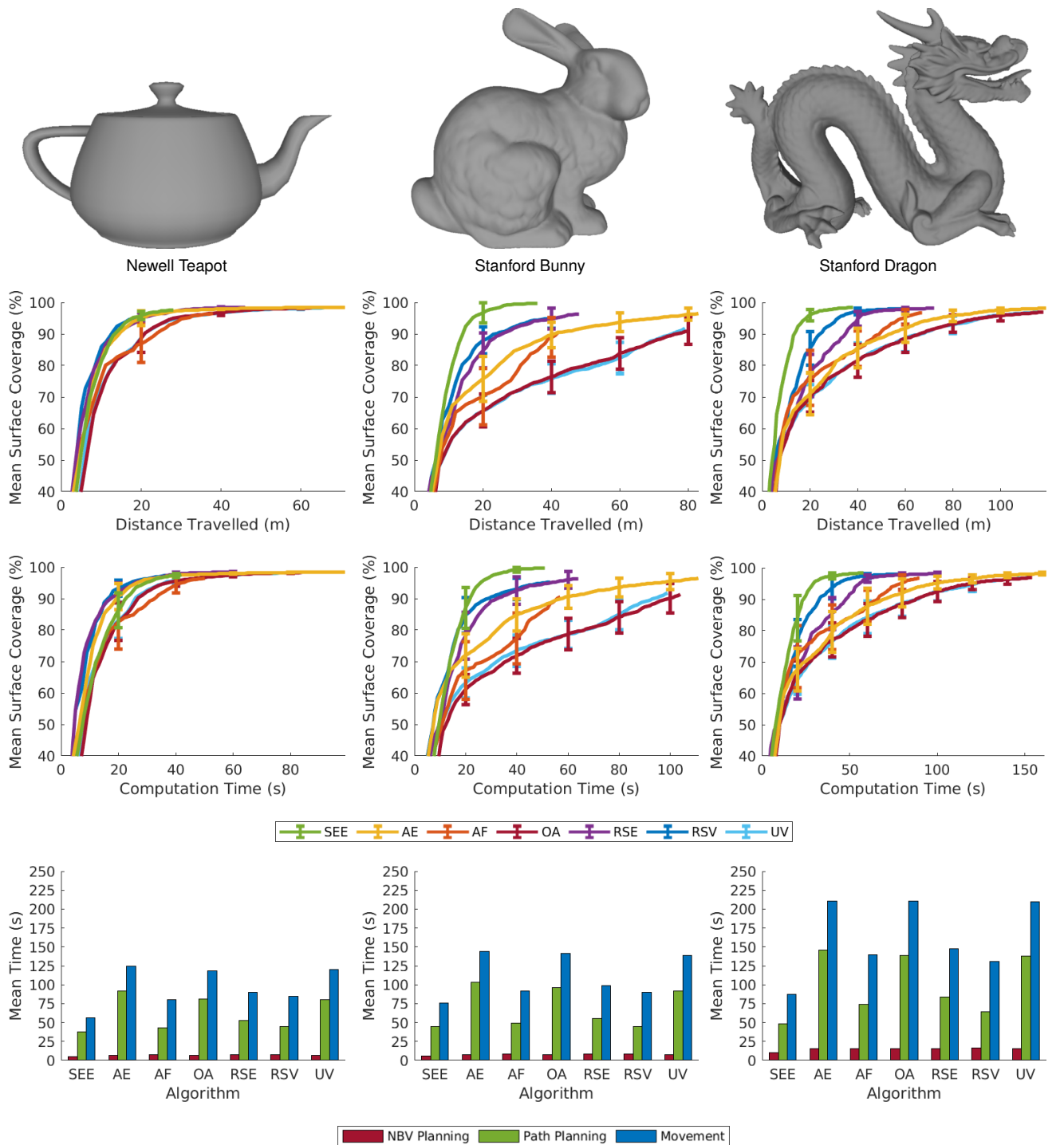


Figure 14. A comparison of SEE and the evaluated volumetric approaches in the UR10 simulation environment for 100 experiments on the Newell Teapot, Stanford Bunny and Stanford Dragon. The graphs show, from top to bottom, the mean surface coverage relative to travel distance, the mean surface coverage relative to computation time (i.e., NBV planning and path planning) and a bar graph of the mean time required for each procedure (i.e., NBV planning, path planning and movement), respectively. The mean surface coverage axes start at 40% to highlight the algorithm performance at completion. The error bars denote one standard deviation around the mean. The table shows each algorithm's final mean number of views, surface coverage, distance travelled and observation time over all 100 experiments on each model, with the best value highlighted in bold.

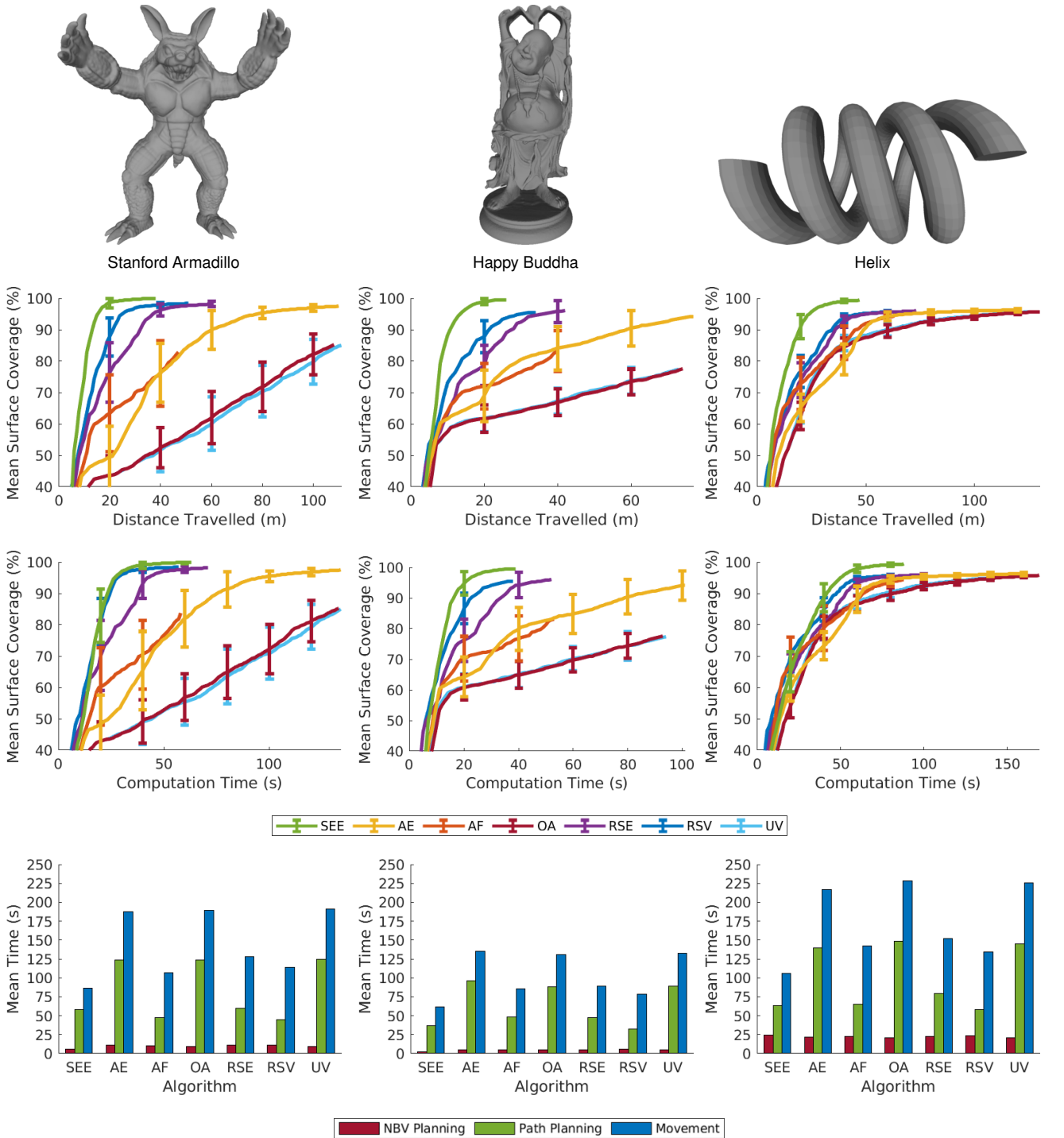


Figure 15. A comparison of SEE and the evaluated volumetric approaches in the UR10 simulation environment for 100 experiments on the Stanford Armadillo, Happy Buddha and Helix. The graphs show, from top to bottom, the mean surface coverage relative to travel distance, the mean surface coverage relative to computation time (i.e., NBV planning and path planning) and a bar graph of the mean time required for each procedure (i.e., NBV planning, path planning and movement), respectively. The mean surface coverage axes start at 40% to highlight the algorithm performance at completion. The error bars denote one standard deviation around the mean. The table shows each algorithm's final mean number of views, surface coverage, distance travelled and observation time over all 100 experiments on each model, with the best value highlighted in bold.

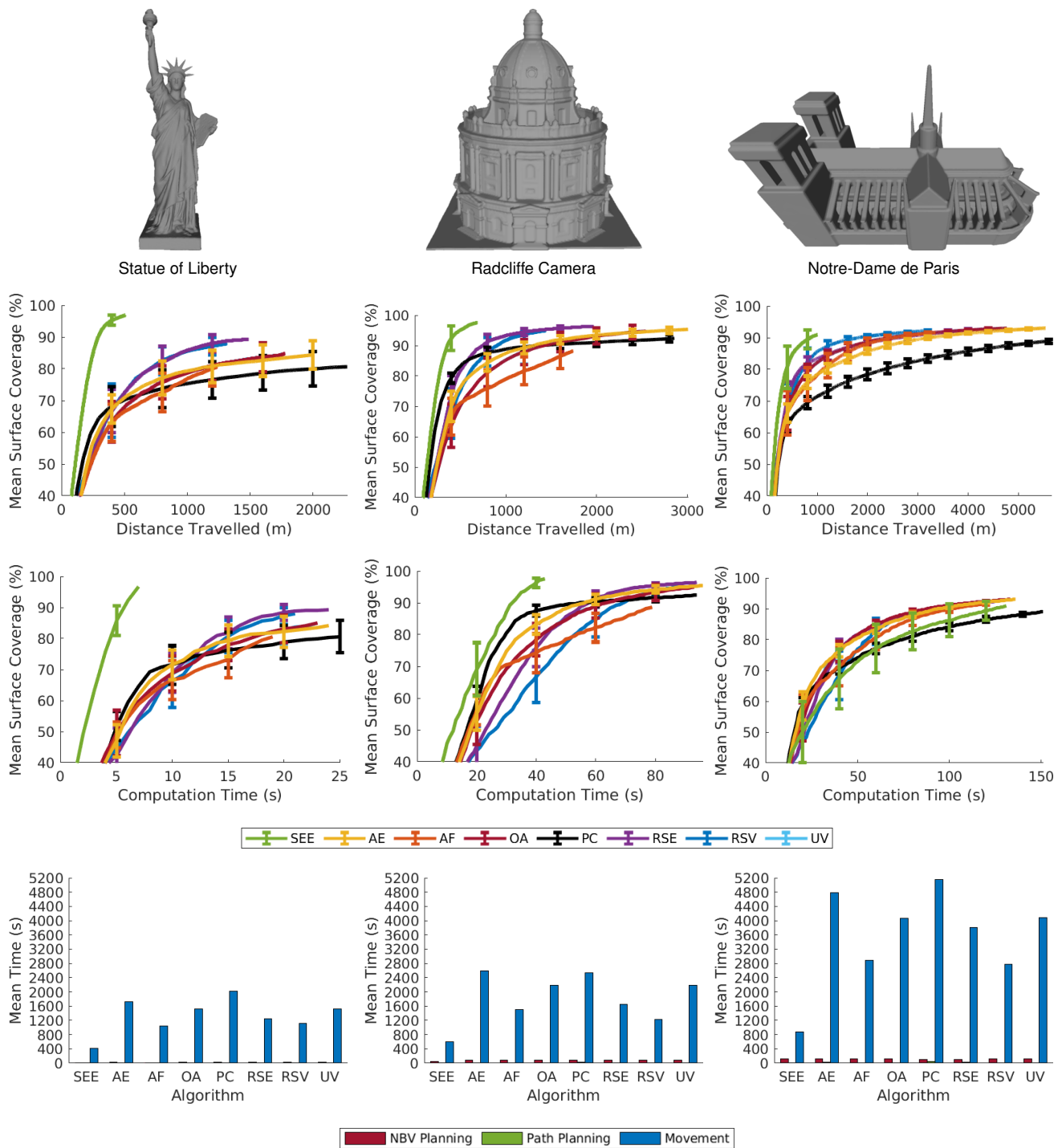


Figure 16. A comparison of SEE and the evaluated volumetric approaches in the UAV simulation environment for 100 experiments on the Statue of Liberty, Radcliffe Camera and Notre-Dame de Paris. The graphs show, from top to bottom, the mean surface coverage relative to travel distance, the mean surface coverage relative to computation time (i.e., NBV planning and path planning) and a bar graph of the mean time required for each procedure (i.e., NBV planning, path planning and movement), respectively. The mean surface coverage axes start at 40% to highlight the algorithm performance at completion. The error bars denote one standard deviation around the mean. The table shows each algorithm's final mean number of views, surface coverage, distance travelled and observation time over all 100 experiments on each model, with the best value highlighted in bold.

Table 4. The field-of-view in degrees, θ_x and θ_y , and resolution in pixels, w_x and w_y , of the Intel RealSense L515 used in the experiments in Section 5.

	Intel RealSense L515	Units
θ_x	70	degrees
θ_y	43	degrees
w_x	640	pixels
w_y	480	pixels

depends upon the surface area of a model relative to the volume of its bounding box. This variation is most noticeable for the AF, OA, UV and PC approaches, which perform significantly worse on models with high surface-to-volume ratios, either locally (e.g., Stanford Bunny ears and Stanford Armadillo limbs) or globally (e.g., the Happy Buddha and Statue of Liberty). These algorithms prioritise voxels that are visible from a previous view, which limits the final surface coverage of objects not easily observed with overlapping views. The PC algorithm is the most affected as it only prioritizes occluded voxels. This made a fair evaluation on the small models unfeasible due to the small viewing frustum of the simulated sensor.

SEE consistently observes all of the models more efficiently than the evaluated volumetric approaches. It obtains equivalent or better observations of every model using fewer views, shorter travel distances and lower observation times. SEE achieves this by proposing and selecting views that obtain greater improvements in surface coverage per unit of distance travelled. The surface coverage obtained per unit of computation time is also frequently higher due to the proactive handling of known occlusions.

5 Real-World Experiments

SEE was deployed on a UR10 robotic arm to evaluate its real-world performance by observing a deer statue, the *Oxford Deer*, for 20 independent experiments. The statistically significant results demonstrate that SEE performs equally well in the real world and captures high-quality observations of the Oxford Deer.

The UR10 platform (Fig. 1) mirrors the UR10 simulation environment, with objects on a turntable being captured by an Intel RealSense L515 (Table 4) affixed to the UR10 end effector. The turntable and UR10 are jointly controlled to obtain a complete observation of the unknown object.

The observation pipeline was extended to handle the noise of a real-world system. Collision-free paths between views were planned with AIT* and executed by MoveIt. The sensor pose was then held steady for 5 seconds before capturing measurements to ensure stability. A radius-based outlier filter was applied to captured measurements to remove sensor noise. These filtered measurements were then aligned to the SEE pointcloud using ICP (Besl and McKay 1992).

SEE used the same user parameters as in simulation (Section 4.2.1) except for the target density, ρ , and the minimum separation distance, ϵ (Table 5). The target density is increased by an order of magnitude and the minimum separation distance is decreased by a similar magnitude in order to capture sufficient measurements on the deer antlers after noise filtering.

Table 5. The parameters used for SEE and the associated analysis in the real-world experiments on the Oxford Deer in Section 5. All the values were user-specified.

	Oxford Deer	Units
ρ	5000000	points per m ³
r	0.03	m
d	0.5	m
ϵ	0.0005	m
ψ	0.5	m
v	0.01	m
τ	100	number of views
η	0.005	m

The real-world performance of SEE is evaluated quantitatively and qualitatively (Fig. 17). Its performance is quantified by surface coverage, view count, travel distance, NBV planning time, path planning time, movement time, measurement time and total observation time. Since there is no ground truth, the surface coverage of each experiment is calculated as a percentage of the final SEE pointcloud. The view count, travel distance, NBV planning time, path planning time and movement time metrics are calculated using the methods presented in Section 4.1. The measurement time combines the sensor steadying time with the time required for noise filtering and applying ICP. The total observation time includes all operations from capturing the first view until SEE finishes an observation. The qualitative performance of SEE is illustrated by the final pointcloud and a mesh reconstruction generated with Open3D (Zhou et al. 2018) for a representative experiment taking the median number of views (Fig. 17, top).

The quantitative results show that SEE was as or more efficient in the real world than in simulation. The Oxford Deer required a similar number of views and movement time to the small model simulation experiments. It required less computation time and travel distance as AIT* found paths that prioritised rotating the turntable over moving the end effector by sampling more goal poses. These paths were simpler and took less planning time to find and resulted in shorter end-effector travel distances. The total observation time is greater since it measures the overall time elapsed between capturing the initial view and SEE completing an observation. This includes measurement time, which was not quantified for the simulation experiments.

The qualitative results show that SEE captured complete and largely accurate observations of the Oxford Deer, despite the presence of sensor noise. The coloured pointcloud (Fig. 17, top center) has high fidelity. This results in a mesh reconstruction (Fig. 17, top right) that is also highly complete and accurate, except for some noise around the face, antlers and hind legs. These quantitative and qualitative results show that SEE is suitable for real robotic scenarios.

6 Conclusion

NBV planning is key to obtaining 3D scene observations. NBV approaches determine where sensor measurements should be captured, with the aim of efficiently obtaining a complete observation. Most existing approaches represent observations by aggregating measurements into an external

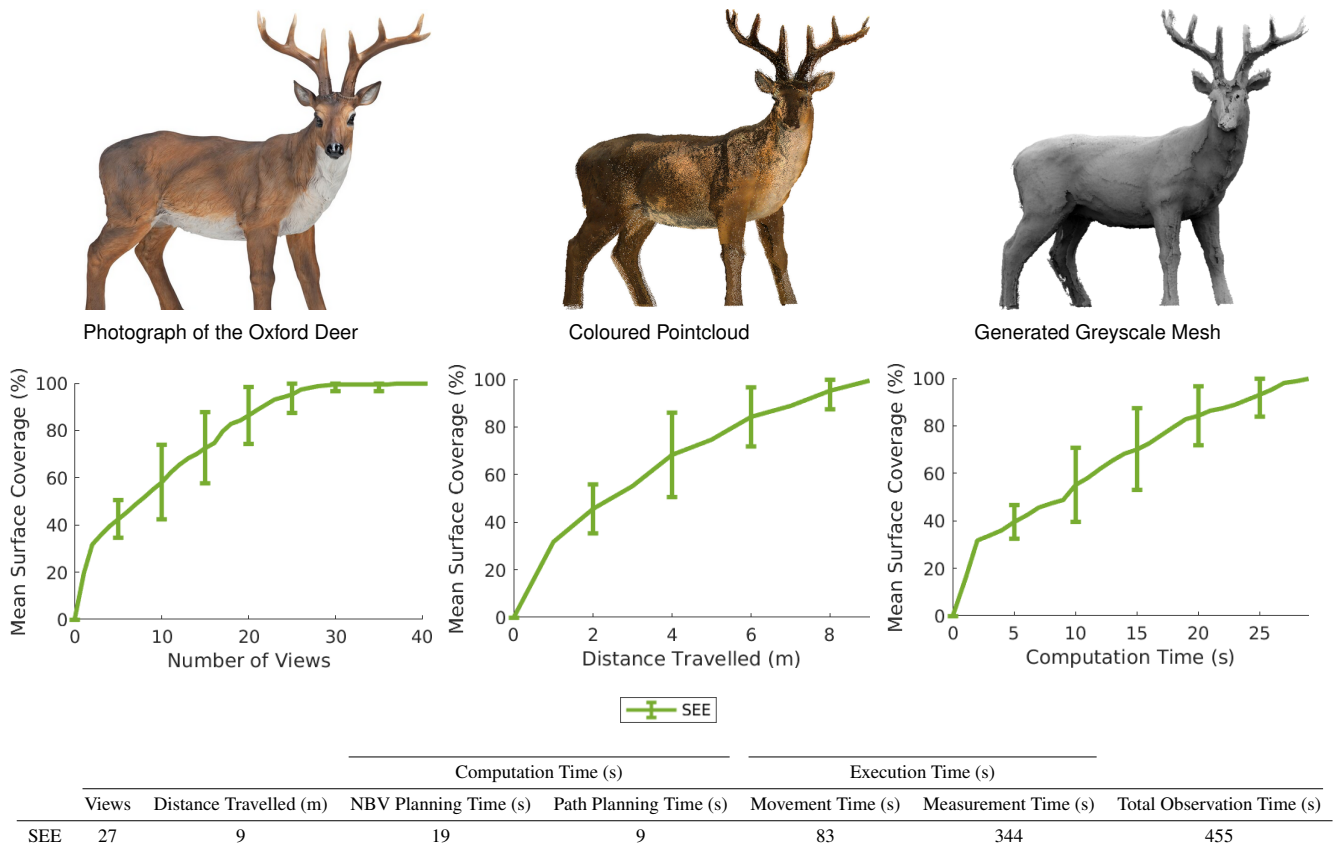


Figure 17. A demonstration of SEE on the UR10 platform for 20 independent experiments observing the Oxford Deer. The images show, from left to right, a photograph of the Oxford Deer, the coloured pointcloud obtained by SEE for a representative run and a greyscale mesh generated from that pointcloud using Open3D, respectively. The graphs show, from left to right, the mean surface coverage relative to the number of views, distance travelled and computation time, respectively. The error bars denote one standard deviation around the mean. The surface coverage is computed relative to the final pointcloud since no ground truth is available. The table shows the final mean number of views captured, distance travelled, NBV planning time, path planning time, movement time, measurement time and total observation time over all 20 experiments.

scene structure. These rigid structures can be easily evaluated but often limit the fidelity of information and are computationally expensive to maintain. This paper presents a NBV approach that overcomes these limitations by using an unstructured density representation.

SEE is a measurement-direct NBV approach that makes view planning decisions directly from sensor measurements to capture a minimum measurement density. Fully and partially observed surfaces are identified by individually classifying each measurement based on the density of neighbouring measurements. Measurements that lie on the boundary between these regions are classified as frontiers. Views are proposed to capture new measurements around these frontier points. These views are initially generated by considering the local surface geometry but can be refined to proactively avoid known occlusions. Observation efficiency is prioritised by choosing next best views to capture the most frontier points while moving short distances. If a view is unsuccessful then it is reactively adjusted to avoid a previously unknown occlusion or surface discontinuity. SEE completes an observation when all frontier points have been observed or are deemed unobservable.

Simulation experiments comparing SEE with state-of-the-art volumetric approaches demonstrate the superior

observation performance of this unstructured measurement-direct NBV approach. SEE is able to obtain highly complete observations of both small- and large-scale scene models while travelling shorter distances and requiring less observation time than the evaluated volumetric approaches. Real-world experiments conducted with a robot arm show that SEE performs equally well in the real world. SEE captured high-quality observations of a deer statue using a UR10 arm with an Intel RealSense L515 sensor.

An open-source implementation of SEE is available at <https://robotic-esp.com/code/see>.

Acknowledgements

The authors would like to thank Wayne Tubby and the Hardware Engineering team at the Oxford Robotics Institute (ORI) for building the UR10 platform used for the real-world experiments.

This research was funded by UK Research and Innovation and EPSRC through Robotics and Artificial Intelligence for Nuclear (RAIN) [EP/R026084/1], ACE-OPS: From Autonomy to Cognitive assistance in Emergency OPERATIONs [EP/S030832/1], and the Autonomous Intelligent Machines and Systems (AIMS) Centre for Doctoral Training (CDT) [EP/S024050/1].

A Index to Multimedia Extensions

The multimedia extensions in Table 6 are available at <https://www.youtube.com/c/roboticesp>.

Table 6. Index to Multimedia Extensions.

Extension	Media Type	Description
1	Video	Simulation experiments on the Newell Teapot
2	Video	Simulation experiments on the Stanford Bunny
3	Video	Simulation experiments on the Stanford Dragon
4	Video	Simulation experiments on the Stanford Armadillo
5	Video	Simulation experiments on the Happy Buddha
6	Video	Simulation experiments on the Helix
7	Video	Simulation experiments on the Statue of Liberty
8	Video	Simulation experiments on the Radcliffe Camera
9	Video	Simulation experiments on the Notre-Dame de Paris
10	Video	Experiment on the UR10 platform

References

- Abduldayem A, Gan D, Seneviratne L and Taha T (2017) 3D Reconstruction of Complex Structures with Online Profiling and Adaptive Viewpoint Sampling. In: *International Micro Air Vehicle Conference and Flight Competition*. pp. 278–285.
- Almadhoun R, Abduldayem A, Taha T, Seneviratne L and Zweiri Y (2019) Guided next best view for 3D reconstruction of large complex structures. *Remote Sensing* 11(20): 1–20. DOI: 10.3390/rs11202440.
- Altman NS (1992) An Introduction to Kernel and Nearest-Neighbor Nonparametric Regression. *The American Statistician* 46(3): 175–185. DOI:10.1080/00031305.1992.10475879.
- Arce S, Vernon CA, Hammond J, Newell V, Janson J, Franke KW and Hedengren JD (2020) Automated 3D reconstruction using optimized view-planning algorithms for iterative development of structure-from-motion models. *Remote Sensing* 12(13). DOI:10.3390/rs12132169.
- Banta JE, Wong LM, Dumont C and Abidi MA (2000) A next-best-view system for autonomous 3-D object reconstruction. *IEEE Transactions on Systems, Man, and Cybernetics* 30(5): 589–598. DOI:10.1109/3468.867866.
- Besl PJ and McKay ND (1992) A Method for Registration of 3-D Shapes. *IEEE Transactions on Pattern Analysis and Machine Intelligence* 14(2): 239–256. DOI:10.1109/34.121791.
- Bircher A, Kamel M, Alexis K, Oleynikova H and Siegwart R (2016) Receding Horizon Next-Best-View Planner for 3D Exploration. In: *IEEE International Conference on Robotics and Automation*. ISBN 9781467380256, pp. 1462–1468. DOI: 10.1109/ICRA.2016.7487281.
- Bircher A, Kamel M, Alexis K, Oleynikova H and Siegwart R (2018) Receding horizon path planning for 3D exploration and surface inspection. *Autonomous Robots* 42(2): 291–306. DOI: 10.1007/s10514-016-9610-0.
- Border R (2019) *Next Best View Planning with an Unstructured Representation*. PhD Thesis, University of Oxford.
- Border R and Gammell JD (2020) Proactive Estimation of Occlusions and Scene Coverage for Planning Next Best Views in an Unstructured Representation. In: *IEEE/RSJ International Conference on Intelligent Robots and Systems*. pp. 1–8.
- Border R, Gammell JD and Newman P (2017) Inferring Surface Geometry from Point Clouds for Next Best View Planning. In: *Joint Industry and Robotics CDTs Symposium*. pp. 1–2.
- Border R, Gammell JD and Newman P (2018) Surface Edge Explorer (SEE): Planning Next Best Views Directly from 3D Observations. In: *IEEE International Conference on Robotics and Automation*. ISBN 9781538630808, pp. 1–8. DOI: 10.1109/ICRA.2018.8461098.
- Boroczyk J (2016) Radcliffe Camera. URL <https://bit.ly/2UZnNkJ>.
- Burkardt J (2012) Helix. URL <https://bit.ly/3h2mkH9>.
- Coleman D, Sucan I, Chitta S and Correll N (2014) Reducing the Barrier to Entry of Complex Robotic Software: a MoveIt! Case Study. *Journal of Software Engineering for Robotics* 5(1): 3–16.
- Connolly CI (1985) The determination of next best views. In: *IEEE International Conference on Robotics and Automation*. ISBN 0818606150, pp. 432–435. DOI:10.1109/ROBOT.1985.1087372.
- Cover H, Choudhury S, Scherer S and Singh S (2013) Sparse Tangential Network (SPARTAN): Motion planning for micro aerial vehicles. In: *IEEE International Conference on Robotics and Automation*. IEEE. ISBN 9781467356411, pp. 2820–2825. DOI:10.1109/ICRA.2013.6630967.
- Curless B and Levoy M (1996) A Volumetric Method for Building Complex Models from Range Images. In: *SIGGRAPH Computer Graphics and Interactive Techniques*. pp. 303–312.
- Daudelin J and Campbell M (2017) An Adaptable, Probabilistic, Next-Best View Algorithm for Reconstruction of Unknown 3-D Objects. *IEEE Robotics and Automation Letters* 2(3): 1540–1547. DOI:10.1109/lra.2017.2660769.
- Delmerico J, Isler S, Sabzevari R and Scaramuzza D (2018) A comparison of volumetric information gain metrics for active 3D object reconstruction. *Autonomous Robots* 42(2): 197–208. DOI:10.1007/s10514-017-9634-0.
- Dierenbach KO, Weinmann M and Jutzi B (2016) Next-Best-View method based on consecutive evaluation of topological relations. In: *International Archives of the Photogrammetry, Remote Sensing and Spatial Information Sciences*, volume 41. pp. 11–19. DOI:10.5194/isprsarchives-XLI-B3-11-2016.
- Drezner Z and Wesolowsky GO (1983) Minimax and maximin facility location problems on a sphere. *Naval Research Logistics* 30(2): 305–312. DOI:10.1002/nav.3800300211.
- Ester M, Kriegel HP, Sander J and Xu X (1996) A Density-Based Algorithm for Discovering Clusters in Large Spatial Databases with Noise. In: *International Conference on Knowledge Discovery and Data Mining*. ISBN 1577350049, pp. 226–231. DOI:10.1.1.71.1980.
- FabShop L (2015) Notre-Dame de Paris. URL <https://bit.ly/378ikR5>.
- Fisher J (2015) Statue of Liberty. URL <https://bit.ly/3jHtb9H>.

- Fritzke B (1994) A Growing Neural Gas Network Learns Topologies. In: *International Conference on Neural Information Processing Systems*, volume 7. ISBN 0691137153, pp. 625–632. DOI:10.1.1.31.4273.
- Hardouin G, Moras J, Morbidi F, Marzat J and Mouaddib EM (2020a) Next-Best-View planning for surface reconstruction of large-scale 3D environments with multiple UAVs. In: *IEEE/RSJ International Conference on Intelligent Robots and Systems*. ISBN 9781728162119, pp. 1567–1574.
- Hardouin G, Morbidi F, Moras J, Marzat J and Mouaddib EM (2020b) Surface-driven Next-Best-View planning for exploration of large-scale 3D environments. In: *21st IFAC World Congress*. pp. 1–8.
- Hollinger GA, Englot BJ, Hover FS, Mitra U and Sukhatme GS (2012) Active planning for underwater inspection and the benefit of adaptivity. *International Journal of Robotics Research* 32(1): 3–18. DOI:10.1177/0278364912467485.
- Hou L, Chen X, Lan K, Rasmussen R and Roberts J (2019) Volumetric Next Best View by 3D Occupancy Mapping Using Markov Chain Gibbs Sampler for Precise Manufacturing. *IEEE Access* 7: 121949–121960. DOI:10.1109/access.2019.2935547.
- Isler S, Sabzevari R, Delmerico J and Scaramuzza D (2016) An Information Gain Formulation for Active Volumetric 3D Reconstruction. In: *IEEE International Conference on Robotics and Automation*. ISBN 9781467380256, pp. 3477–3484. DOI:10.1109/ICRA.2016.7487527.
- Karaman S and Frazzoli E (2011) Sampling-based Algorithms for Optimal Motion Planning. *International Journal of Robotics Research* 30(7): 846–894. DOI:10.1177/0278364911406761.
- Karaszewski M, Adamczyk M and Sitnik R (2016a) Assessment of next-best-view algorithms performance with various 3D scanners and manipulator. *ISPRS Journal of Photogrammetry and Remote Sensing* 119: 320–333. DOI:10.1016/j.isprsjprs.2016.06.015.
- Karaszewski M, Sitnik R and Bunsch E (2012) On-line, collision-free positioning of a scanner during fully automated three-dimensional measurement of cultural heritage objects. *Robotics and Autonomous Systems* 60(9): 1205–1219. DOI:10.1016/j.robot.2012.05.005.
- Karaszewski M, Stępień M and Sitnik R (2016b) Two-stage automated measurement process for high-resolution 3D digitization of unknown objects. *Applied Optics* 55(29): 8162–8170. DOI:10.1364/AO.55.008162.
- Katz S, Tal A and Basri R (2007) Direct visibility of point sets. *ACM Transactions on Graphics* 26(3): 24. DOI:10.1145/1276377.1276407.
- Kavraki LE, Švestka P, Latombe JC and Overmars MH (1996) Probabilistic roadmaps for path planning in high-dimensional configuration spaces. *IEEE Transactions on Robotics and Automation* 12(4): 566–580. DOI:10.1109/70.508439.
- Kazhdan M, Bolitho M and Hoppe H (2006) Poisson Surface Reconstruction. In: *Eurographics Symposium on Geometry Processing*. pp. 1–13.
- Khalfaoui S, Seulin R, Fougerolle Y and Fofi D (2013) An efficient method for fully automatic 3D digitization of unknown objects. *Computers in Industry* 64(9): 1152–1160. DOI:10.1016/j.compind.2013.04.005.
- Krainin M, Curless B and Fox D (2011) Autonomous generation of complete 3D object models using next best view manipulation planning. In: *IEEE International Conference on Robotics and Automation*. ISBN 9781612843865, pp. 5031–5037. DOI:10.1109/ICRA.2011.5980429.
- Kriegel S, Bodenmüller T, Suppa M and Hirzinger G (2011) A Surface-Based Next-Best-View Approach for Automated 3D Model Completion of Unknown Objects. In: *IEEE International Conference on Robotics and Automation*. ISBN 9781612843803, pp. 4869–4874. DOI:10.1109/ICRA.2011.5979947.
- Kriegel S, Rink C, Bodenmüller T, Narr A, Suppa M and Hirzinger G (2012) Next-best-scan planning for autonomous 3D modeling. In: *IEEE International Conference on Intelligent Robots and Systems*. ISBN 9781467317375, pp. 2850–2856. DOI:10.1109/IROS.2012.6385624.
- Kriegel S, Rink C, Bodenmüller T and Suppa M (2015) Efficient next-best-scan planning for autonomous 3D surface reconstruction of unknown objects. *Journal of Real-Time Image Processing* 10(4): 611–631. DOI:10.1007/s11554-013-0386-6.
- Krishnamurthy V and Levoy M (1996) Fitting smooth surfaces to dense polygon meshes. In: *Conference on Computer Graphics and Interactive Techniques*. ISBN 0897917464, pp. 313–324. DOI:10.1145/237170.237270.
- Lauri M, Pajarinen J, Peters J and Frintrop S (2019) Approximation of joint information gain for multi-sensor volumetric scene reconstruction. In: *2nd Workshop on Informative Path Planning and Adaptive Sampling*. pp. 1–8.
- Lauri M, Pajarinen J, Peters J and Frintrop S (2020) Multi-sensor next-best-view planning as matroid-constrained submodular maximization. *IEEE Robotics and Automation Letters* 5(4): 5323–5330. DOI:10.1109/LRA.2020.3007445.
- LaValle SM (1998) Rapidly-Exploring Random Trees: A New Tool for Path Planning. Technical report, Iowa State University, Ames.
- Low KL and Lastra A (2006) Efficient constraint evaluation algorithms for hierarchical next-best-view planning. In: *Symposium on 3D Data Processing, Visualization, and Transmission*. ISBN 0769528252, pp. 830–837. DOI:10.1109/3DPVT.2006.52.
- Massios NA and Fisher RB (1998) A Best Next View Selection Algorithm Incorporating a Quality Criterion. In: *British Machine Vision Conference*. pp. 780–789. DOI:10.1.1.41.3293.
- Mendoza M, Irving Vazquez-Gomez J, Taud H, Sucar LE, Reta C, Vazquez-Gomez JI, Taud H, Sucar LE and Reta C (2020) Supervised learning of the next-best-view for 3d object reconstruction. *Pattern Recognition Letters* 133: 224–231. DOI:10.1016/j.patrec.2020.02.024.
- Monica R and Aleotti J (2018a) Contour-based next-best view planning from point cloud segmentation of unknown objects. *Autonomous Robots* 42(2): 443–458. DOI:10.1007/s10514-017-9618-0.
- Monica R and Aleotti J (2018b) Surfel-Based Next Best View Planning. *IEEE Robotics and Automation Letters* 3(4): 3324–3331. DOI:10.1109/LRA.2018.2852778.
- Newell ME (1976) *The utilization of procedure models in digital image synthesis*. PhD Thesis, University of Utah.
- Palomeras N, Hurtos N, Vidal E and Carreras M (2019) Autonomous exploration of complex underwater environments using a probabilistic next-best-view planner. *IEEE Robotics*

- and *Automation Letters* 4(2): 1619–1625. DOI:10.1109/LRA.2019.2896759.
- Papadopoulos-Orfanos D and Schmitt F (1997) Automatic 3-D digitization using a laser rangefinder with a small field of view. In: *International Conference on Recent Advances in 3-D Digital Imaging and Modeling*. ISBN 0-8186-7943-3, pp. 60–67. DOI:10.1109/IM.1997.603849.
- Patel MH and Chidambaram A (2002) A new method for minimax location on a sphere. *International Journal of Industrial Engineering: Theory Applications and Practice* 9(1): 96–102.
- Peng C and Isler V (2019) Adaptive View Planning for Aerial 3D Reconstruction. In: *IEEE International Conference on Robotics and Automation*. pp. 2981–2987.
- Peralta D, Casimiro J, Nilles AM, Aguilar JA, Atienza R and Cajote R (2020) Next-Best View Policy for 3D Reconstruction. In: *ECCV 2020 Workshops*. pp. 1–16.
- Potthast C and Sukhatme GS (2011) Next best view estimation with eye in hand camera. In: *International Conference on Intelligent Robots and Systems*. pp. 1–4.
- Potthast C and Sukhatme GS (2014) A probabilistic framework for next best view estimation in a cluttered environment. *Journal of Visual Communication and Image Representation* 25(1): 148–164. DOI:10.1016/j.jvcir.2013.07.006.
- Reed MK and Allen PK (2000) Constraint-based sensor planning for scene modeling. *IEEE Transactions on Pattern Analysis and Machine Intelligence* 22(12): 1460–1467. DOI:10.1109/34.895979.
- Roberts M, Truong A, Dey D, Sinha S, Kapoor A, Joshi N and Hanrahan P (2017) Submodular Trajectory Optimization for Aerial 3D Scanning. *International Conference on Computer Vision* : 5334–5343.
- Rodrigues O (1840) Des Lois Geometriques Qui Regissent les Deplacements d'un Systeme Solide dans L'espace, et de la Variation des Coordonnees Provenant de ces Deplacements Consideres dependamment des Causes Qui Peuvent les Produire. *Journal de Mathématiques Pures et Appliquées* 5(1840): 380–440.
- Schmid L, Pantic M, Khanna R, Ott L, Siegwart R and Nieto J (2019) An efficient sampling-based method for online informative path planning in unknown environments. *IEEE Robotics and Automation Letters* 5(2): 1500–1507.
- Scott WR, Roth G and Rivest JF (2003) View planning for automated three-dimensional object reconstruction and inspection. *ACM Computing Surveys* 35(1): 64–96. DOI: 10.1145/641865.641868.
- Selin M, Tiger M, Duberg D, Heintz F and Jensfelt P (2019) Efficient autonomous exploration planning of large-scale 3-d environments. *IEEE Robotics and Automation Letters* 4(2): 1699–1706. DOI:10.1109/LRA.2019.2897343.
- Song S and Jo S (2017) Online inspection path planning for autonomous 3D modeling using a micro-aerial vehicle. In: *IEEE International Conference on Robotics and Automation*. ISBN 9781509046331, pp. 6217–6224. DOI:10.1109/ICRA.2017.7989737.
- Song S and Jo S (2018) Surface-Based Exploration for Autonomous 3D Modeling. In: *IEEE International Conference on Robotics and Automation*. ISBN 9781538630808, pp. 1–8. DOI: 10.1109/icra.2018.8460862.
- Song S, Kim D and Jo S (2020) Online coverage and inspection planning for 3D modeling. *Autonomous Robots* 44(8): 1431–1450. DOI:10.1007/s10514-020-09936-7.
- Strub MP and Gammell JD (2020) Adaptively Informed Trees (AIT*): Fast Asymptotically Optimal Path Planning through Adaptive Heuristics. In: *IEEE International Conference on Robotics and Automation*. ISBN 9781728173955, pp. 3191–3198. DOI:10.1109/ICRA40945.2020.9197338.
- Strub MP and Gammell JD (2022) AIT* and EIT*: Asymmetric bidirectional sampling-based path planning. *The International Journal of Robotics Research* .
- Sucan I, Moll M and Kavraki LE (2012) The Open Motion Planning Library (OMPL). *IEEE Robotics & Automation Magazine* 19(December): 72–82.
- Tarabanis KA, Allen PK and Tsai RY (1995) A Survey of Sensor Planning in Computer Vision. *IEEE Transactions on Robotics and Automation* 11(1): 86–104.
- Turk G and Levoy M (1994) Zippered polygon meshes from range images. In: *SIGGRAPH Computer Graphics and Interactive Techniques*. ISBN 0-89791-667-0, pp. 311–318. DOI:10.1145/192161.192241.
- Vasquez-Gomez JI, Lopez-Damian E and Sucar LE (2009) View planning for 3D object reconstruction. In: *International Conference on Intelligent Robots and Systems*. ISBN 9781424438044, pp. 4015–4020. DOI:10.1109/IROS.2009.5354383.
- Vasquez-Gomez JI, Sucar LE and Murrieta-Cid R (2017) View/state planning for three-dimensional object reconstruction under uncertainty. *Autonomous Robots* 41(1): 89–109. DOI:10.1007/s10514-015-9531-3.
- Vasquez-Gomez JI, Sucar LE, Murrieta-Cid R and Herrera-Lozada JC (2018) Tree-based search of the next best view/state for three-dimensional object reconstruction. *International Journal of Advanced Robotic Systems* 15(1): 1–11. DOI:10.1177/1729881418754575.
- Vasquez-Gomez JI, Sucar LE, Murrieta-Cid R and Lopez-Damian E (2014) Volumetric Next Best View Planning for 3D Object Reconstruction with Positioning Error. *International Journal of Advanced Robotic Systems* 11(10): 159. DOI:10.5772/58759.
- Wang Y, James S, Stathopoulou EK, Beltran-Gonzalez C, Konishi Y and Del Bue A (2019) Autonomous 3-D Reconstruction, Mapping, and Exploration of Indoor Environments with a Robotic Arm. *IEEE Robotics and Automation Letters* 4(4): 3340–3347. DOI:10.1109/LRA.2019.2926676.
- Wong LM, Dumont C and Abidi MA (1999) Next Best View System in a 3-D Object Modeling Task. In: *International Symposium on Computational Intelligence in Robotics and Automation*. ISBN 0780358066, pp. 306–311. DOI:10.1109/CIRA.1999.810066.
- Yoder L and Scherer S (2016) Autonomous Exploration for Infrastructure Modeling with a Micro Aerial Vehicle. *Field and Service Robotics* 10: 427–440. DOI:10.1007/978-3-319-27702-8_28.
- Zeng R, Wen Y, Zhao W and Liu YJ (2020) View planning in robot active vision: A survey of systems, algorithms, and applications. *Computational Visual Media* 6(3): 225–245. DOI:10.1007/s41095-020-0179-3.
- Zhou QY, Park J and Koltun V (2018) Open3D: A Modern Library for 3D Data Processing. *arXiv:1801.09847* .